Mapping Composition-Selectivity Relationships of Supported Sub-10 nm Cu-Ag Nanocrystals for High-Rate CO$_2$ Electroreduction

Daniel Choukroun,[*, §] *Lien Pacquets,*[§,||] *Chen Li,*[||] *Saskia Hoekx,*[§,||] *Sven Arnouts,*[§,||] *Kitty Baert,*[#] *Tom Hauffman,*[#] *Sara Bals,*[||] *Tom Breugelmans*[*,§,‡]

[§]Applied Electrochemistry and Catalysis (ELCAT), University of Antwerp, 2610 Wilrijk, Belgium

[||]Electron Microscopy for Materials Research (EMAT), University of Antwerp, 2020 Antwerp, Belgium

[#]Electrochemical and Surface Engineering (SURF), Materials and Chemistry (MACH), Vrije Universiteit Brussel, Pleinlaan 2, 1050 Brussels, Belgium

[‡]Separation & Conversion Technologies, Flemish Institute for Technological Research (VITO), 2400 Mol, Belgium

*Corresponding authors: Daniel.Choukroun@uantwerpen.be , Tom.Breugelmans@uantwerpen.be

ABSTRACT

Colloidal Cu-Ag nanocrystals measuring less than 10 nanometer across are promising candidates for integration in hybrid CO_2 reduction reaction interfaces, especially in the context of tandem catalysis and selective multicarbon (C_2-C_3) product formation. In this work, we vary the synthetic ligand-to-copper molar ratio from 0.1 to 1.0 and the silver-to-copper atomic ratio from zero to 0.7 and study the variations in the nanocrystals' size distribution, morphology and reactivity at rates $>=$ 100 mA cm^{-2} in a gas-fed recycle electrolyzer operating under neutral to mildly basic conditions (0.1-1.0 M $KHCO_3$). High-resolution electron microscopy and spectroscopy are used in order to characterize the morphology of *sub*-10-nm Cu-Ag nanodimers and core-shells and to elucidate trends in Ag coverage and surface composition. It is shown that Cu-Ag nanocrystals can be densely dispersed onto a carbon black support without the need for immediate ligand removal or binder addition, which facilitates their application considerably. Although CO_2RR product distribution remains an intricate function of time, (kinetic) overpotential and processing conditions, we nevertheless conclude that the ratio of oxygenates to hydrocarbons – which depends primarily on the initial dispersion of the nanocrystals and their composition - rises threefold at moderate Ag at.% relative to Cu NCs-based electrodes. Finally, the merits of this particular Cu-Ag/C system and the recycle reactor employed are utilized to obtain maximum C_2-C_3 partial current densities of 92-140 mA cm^{-2} at -1.15 V_{RHE} and liquid product concentrations in excess of 0.05 wt.% in 1 M $KHCO_3$ after short electrolysis periods.

KEYWORDS: copper, silver, nanocrystals, nanodimers, core-shells, CO_2 electroreduction, multicarbon products

The prospect of harnessing solar energy to drive the electrochemical reduction of carbon dioxide (CO_2RR) into chemical building blocks and liquid fuels[1-6] has accelerated research into a plethora of Cu-based mono- and bimetallic catalytic architectures, which along with tailored processing conditions, have pushed selectivity and energy efficiency towards new heights.[7-16] Among those architectures, bimetallic Cu-based systems[17-19] provide a means for modifying the local atomic coordination and thus the electronic properties of Cu surface atoms through variation of the elemental composition. Faceting, size[20-22] and the immediate environment of Cu atoms then dictate the governing CO_2RR mechanism and the corresponding binding energies of important intermediates such as *COCHO[23-24]/*COH or *COCOH/*CH_2CHO[25-26] in the C_2 pathways to ethylene and ethanol. Notably, Cu-Ag surfaces reduce carbon dioxide and carbon monoxide towards oxygenates more selectively than metallic Cu surfaces. This has been attributed in the literature to surface alloying and a modified electronic structure on the one hand,[27-29] and to the presence of a multitude of grain boundaries and interfaces between segregated Cu-Ag domains on the other hand.[30-32]

In the special case of small Cu-Ag nanocrystals (NCs) capped by organic ligands, segregation is attributed to the higher surface energy of Cu and the requirement of reducing surface strain. That forces Ag atoms to adopt a segregated configuration in the form of Janus structures or core@shells, which lowers the energy of the system.[33-35] In the effort to tailor the size, morphology and thus catalytic properties of such NCs, colloidal methods that employ organic ligands such as tetradecylphosphonic acid (TDPA)[36-38] have proven invaluable, also in the rich context of CO_2RR research.[39-40]

However, only a handful of studies dealt with the performance of bimetallic Cu-Ag nanocrystals[41-43] and to date, none had explored the performance of *sub*-10-nm TDPA-capped Cu-Ag NCs at current densities $\geq$ 100 mA cm^{-2}. Such NCs have the important advantage of being deployable in a variety of doped-carbon/metal gas-diffusion-electrode-based reaction

interfaces that in turn hold promise both from a process-minded (tuning local feed concentrations, partial pressure gradients) and catalyst-minded (particle stabilization, confinement) approaches.[44-48]

It is generally accepted that TDPA does not play a role in enhancing CO_2 reduction selectivity under typical reaction conditions,[49-50] unlike amine-containing organic additives[51-52] and cationic surfactants[53-54] for instance. Nevertheless, ligand concentration affects the size distribution and morphology of Cu-Ag NCs,[55-56] and therefore dictates the spatial distribution of Ag atoms at the surface, irrespective of the Ag/Cu ratio. That, we hypothesized, could have a measurable impact on CO_2RR product distribution, provided that both Cu and Ag active sites are exposed and that the proximity between them is maintained after coating and polarization. In what follows, we explore that hypothesis by mapping the composition-selectivity relationships of unsupported and supported Cu-Ag NCs (0-41 at.%) under various processing conditions, while studying the dynamic response of both catalyst and system variables, in an attempt to deconvolute intrinsic catalytic behavior from ligand or reactor-related phenomena.

RESULTS AND DISCUSSION

Morphological Differences between Cu-Ag nanocrystals

The distinct color of *sub*-10-nm Cu and Cu-Ag NCs suspensions is, to the naked eye, the most accessible qualitative indicator of particle size, composition and morphology, as can be appreciated from **Figures S.1-S.2**. That optical behavior stems from the NCs' surface chemistry and from the different dielectric functions of Cu and Ag in the UV-Vis region of the electromagnetic spectrum,[57-59] as indicated by the changes in position and intensity of local surface plasmon resonance (LSPR) bands in the optical spectra of Cu and Cu-Ag NCs (**Figure S.3**). However, delicate morphological changes to particle size and particle elongation, and the discrimination between *sub*-10-nm nanodimers and core-shells can only be assessed by transmission electron microscopy, notably in HAADF-STEM mode. Because electron scattering in this mode is strongly dependent on the atomic number Z, changes in intensity across a particle can be correlated to its composition.[60-61] Given the large difference in atomic number between Cu (Z=29) and Ag (Z=47), Ag-rich regions appear slightly brighter relative to the underlying or adjacent Cu NCs, of which overview HAADF-STEM images are depicted in **Figure 1a-c**. **Figure 1d-f** shows that the NCs' diameter can be tuned between 6.4 nm and 12.2 nm (standard deviation ~6-11%) by varying the synthetic ligand-to-copper (P/Cu) molar ratio between 0.1 and 1.0 equivalents. At 0.1 equivalents, one obtains in fact a mixture of post- and *sub*-10-nm NCs (**Figure S.4**) that can be size-separated by centrifugation, thus yielding the NCs shown in **Figure 1a**. It is important to note that fine adjustment of NC diameter in the aforementioned size range can also be achieved by varying the duration of nucleation or growth periods. In this paper, we chose to focus on Cu-Ag NCs that were prepared from *sub*-10-nm Cu NC precursors, *i.e.* having synthetic P/Cu ratios of either 0.1 or 0.5. An overview of the synthetic scheme leading to the formation of those Cu-Ag NCs is provided in **Figure S.5**.

Next, **Figure 2** presents HAADF-STEM overview images of four batches: **Cu/Ag$_{0.14}$**, **Cu@Ag$_{0.17}$**, **Cu/Ag$_{0.23}$** and **Cu@Ag$_{0.41}$** that were formed by reacting Cu NCs with a varying amount of Ag, either in one or two galvanic replacement (GR) steps.
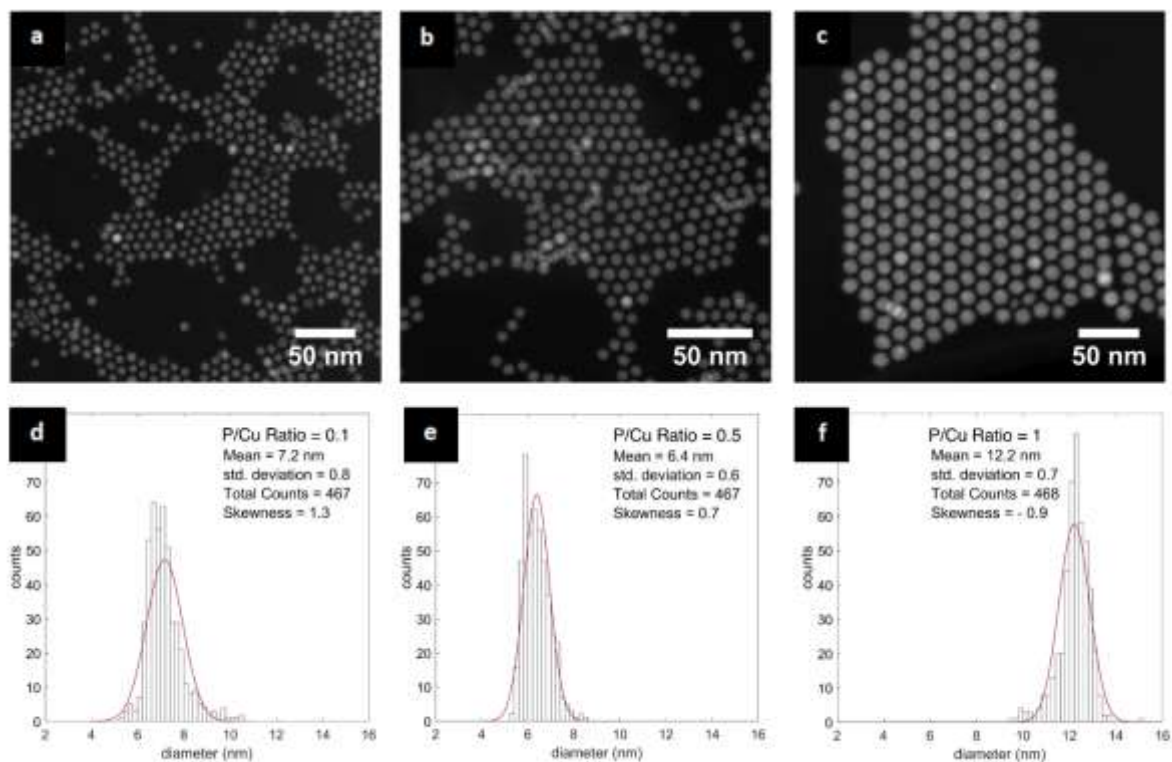
Figure 1 HAADF-STEM images of Cu NCs with P/Cu ratios of (a) 0.1 (size-selected by centrifugation) (b) 0.5 and (c) 1.0. Corresponding histograms and particle size distributions are shown in panel d-f, respectively.
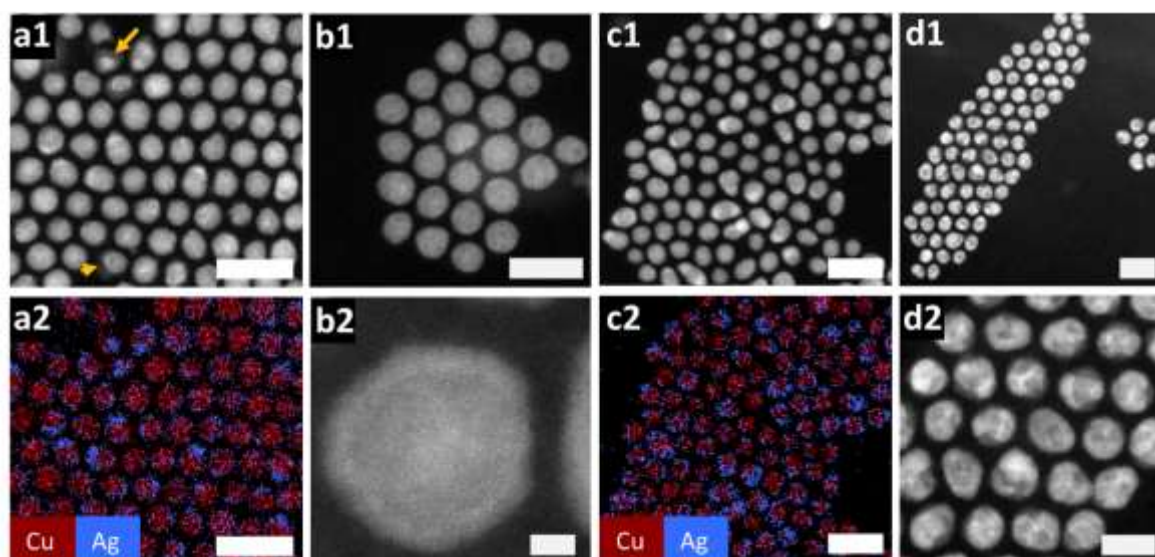
*Figure 2 HAADF-STEM overview images of (a1) **Cu/Ag$_{0.14}$** (b1) **Cu@Ag$_{0.17}$** (c1) **Cu/Ag$_{0.23}$** and (d1) **Cu@Ag$_{0.41}$**. Scale bars: 20 nm. (a2) EDX mapping of **Cu/Ag$_{0.14}$** , scale bar: 20 nm (b2) high-magnification HAADF-STEM image of **Cu@Ag$_{0.17}$**, scale bar: 2 nm (c2) EDX mapping of **Cu/Ag$_{0.23}$** , scale bar: 20 nm and (d2) high-magnification HAADF-STEM image of **Cu@Ag$_{0.41}$**, scale bar: 10 nm. The yellow arrows in Figure 2a1 show sporadic Cu leaching and structure inversion to Ag@Cu$_2$O, due to O$_2$ exposure in the process of grid pretreatment (See Methods).*

EDX maps and high-magnification HAADF-STEM images (**Figure 2-a2-d2**) show unambiguously that mixtures of Cu-Ag nanodimers and core-shells, having mean diameters in the range of 6.4 nm to 8.9 nm, were formed (see **Figure S.6-S.9** for histograms).

It can be noticed that **Cu@Ag$_{0.17}$** has a pronounced core-shell morphology and the largest area-equivalent diameter of the series. The two properties are related: as the diameter of Cu NCs surpasses ~8 nm, much better wettability by Ag is observed even after a single GR step, similar to 11-15 nm TDPA or oleylamine-capped Cu@Ag particles that were previously reported in the literature.[62-63] That discrepancy in wettability can be explained by the difference in interfacial energy (γ_{int}), which scales with the Cu-Ag interfacial area and thus with the initial Cu NC size. As γ_{int} is lower for **Cu@Ag$_{0.17}$** when compared to **Cu/Ag$_{0.14}$** and **Cu/Ag$_{0.23}$**, core-shell formation becomes thermodynamically favorable over nanodimer formation as $\gamma_{Cu} > \gamma_{int} + \gamma_{Ag}$.[64-65]

Spectroscopic and Electrochemical Characterization of As-prepared Cu-Ag NCs

XPS was utilized in order to probe the composition of the outermost surface layers of drop-cast NC films and assess macroscopic trends in Ag surface coverage. Elemental compositions were calculated as described in the Methods section from high-resolution Cu$2p$, Ag$3d$ and O$1s$ spectra, which are shown in **Figure S.10**. In general, surface compositions were found to be higher than the bulk compositions that were measured by ICP-MS or EDX (Table 1).

Table 1 *Properties of the main Cu/Ag and Cu@Ag batches sorted according to their morphologies and bulk Cu atomic percentage*

Catalyst	d_p* (nm)	Bulk Cu at.%** (EDX/ICP-MS)	Bulk Ag at.%** (EDX/ICP-MS)	Surface Cu at.% (XPS)	Surface Ag at.% (XPS)	P/Cu (EDX)	Morphology
Cu/Ag$_{0.14}$	6.4 ± 0.6	86.2	13.8	81.4	18.6	0.05	nanodimers
Cu/Ag$_{0.23}$	6.8 ± 0.8	77.0	23.0	67.6	32.4	0.06	nanodimers
Cu@Ag$_{0.17}$	8.9 ± 0.9	82.6	17.4	64.8	35.2	0.02	Core@Shell
Cu@Ag$_{0.41}$	7.5 ± 0.5	58.8	41.2	37.9	62.1	0.05	Core@Shell

* $\mu \pm \sigma$; ** EDX/ICP-MS

The abovementioned differences in shell morphology and surface composition did not manifest themselves in the position of the Ag $3d_{5/2}$ core-level peak, which is centered at 368.2-368.3 eV (**Figure 3a** and **Table S.1**). The lack of a significant chemical shift, *e.g.* as reported by Dettelbach,[66] rules out bulk alloying in the samples. Moreover, the asymmetrical peak shape and minor loss features observed are indicative of metallic Ag.

X-ray induced Auger lines (Cu $L_3M_{4,5}M_{4,5}$) show a distinctive Cu(0) feature at 918.6 eV for a range of Cu-Ag NCs (**Figure 3b**). Deconvolution is required in order to assess the relative contributions of Cu(0), Cu(I) and Ag(0) to the spectrum, but it is complicated by the fact that multiple peaks are needed to fit even a pure Cu (**Figure S.11a**) or Cu$_2$O CuLMM spectrum.[67] Using the experimentally obtained properties of the Ag $3p_{3/2}$ peak (**Figure S.11b**) and surface

compositions mentioned earlier we could nevertheless obtain rough estimates of the Cu(0) and Cu(I) contributions in **Cu/Ag0.14** and **Cu/Ag0.23** (**Figure S.12** and **Table S.1**). That analysis proved that the chemical state of the NCs was predominantly metallic. In contrast, higher contributions of Cu(I) were measured over (i) **Cu/Ag0.15** (*vide infra*) and (ii) **Cu@Ag0.54**, a morphological analogue of **Cu@Ag0.41** that was employed as XPS reference only. In general, the higher Cu(I) contribution at the surface of Cu-Ag NCs-based films could be attributed to Ag@Cu$_2$O inversion upon O$_2$ exposure, as was highlighted in **Figure 2a1**, or to Cu leaching in suspension, as **Figure S.13** shows for **Cu@Ag0.54**.
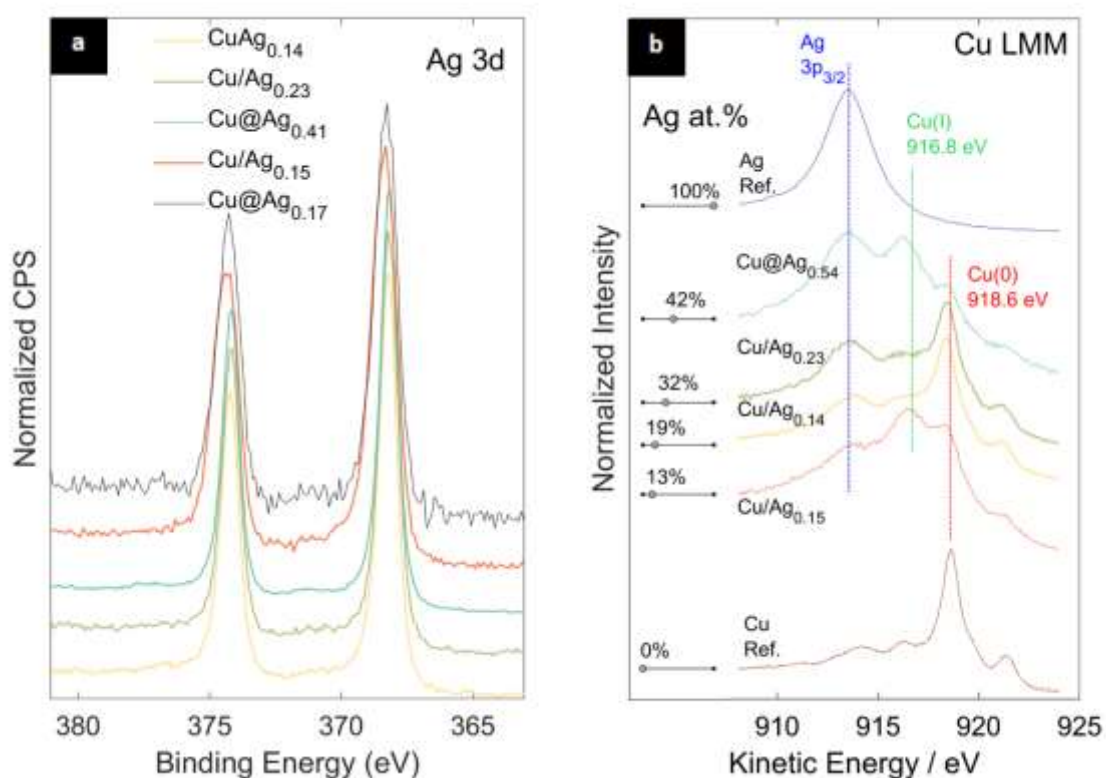
Figure 3 *(a) XPS Ag 3d spectra of Cu-Ag NCs and (b) Cu LMM spectra showing contribution from Ag3p. Reference spectra of Cu and Ag foils are also provided. The corresponding Ag surface composition is given to the left of the spectra.*

Consequently, we used voltammetry and the CO_2RR reaction itself to probe the surface of the NCs. To that end, Cu-Ag NCs were drop-cast onto gas diffusion electrodes (GDEs) under inert atmosphere and exposed only briefly to air before electrolysis. Then, chronopotentiometric CO_2 reduction experiments were performed at 100 mA cm^{-2} using a recycle electrolyzer system (**Figure S.14**) in a 0.1 M $CsHCO_3$ electrolyte. The latter was chosen because of its promoting role in multicarbon and carbon monoxide formation over Ag and Cu surfaces.[68] **Figure 4** shows that the transition from partial (nanodimer) to complete (core@shell) coverage of the Cu cores by Ag was accompanied by an increase of CO_2RR selectivity towards carbon monoxide, the major product formed over Ag surfaces.[69-73] While **Cu@Ag0.41** recorded the highest CO selectivity (83.8%) at -1.2 V_{RHE} (**Table S.2**), **Cu@Ag0.17** lagged not far behind with 82.5% at -1.14 V_{RHE}. Liquid product analysis by HPLC (See **Figure S.15-S.16**) revealed that several C_2 and C_3 products, such as ethanol, acetate and n-propanol, were formed over **Cu/Ag0.14** and to a lesser extent over **Cu@Ag0.17,** whereas formate was the only measurable liquid product in experiments involving **Cu@Ag0.41** electrodes. That CO_2RR performance was rationalized in
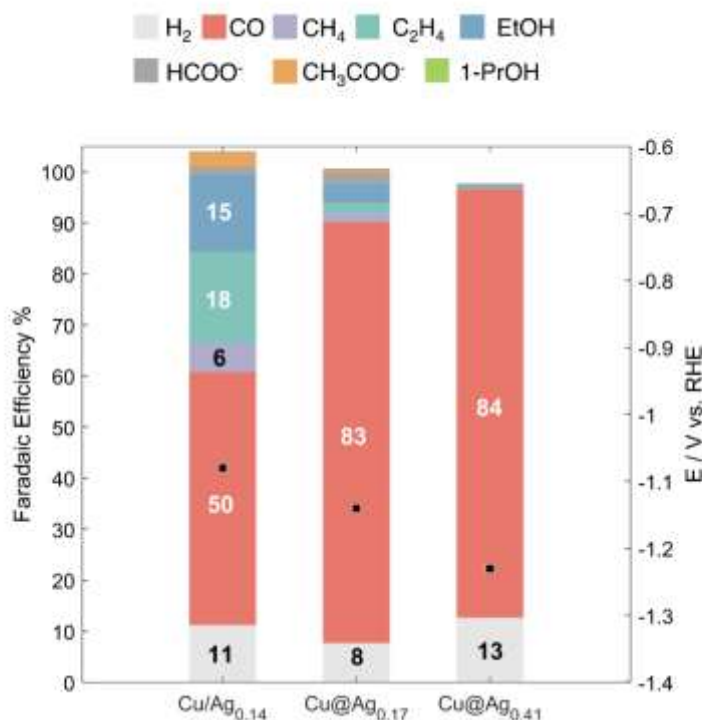

Figure 4 *CO_2RR selectivity of as-prepared Cu-Ag NCs-based gas diffusion electrodes at 0.1A cm^{-2} in 0.1M $CsHCO_3$.*

part by the differences in the voltammetric behavior of Cu and Cu-Ag-NCs-based electrodes (**Figure S.17-S.18**), which pointed in favor of either gradual Ag enrichment at the surface or a steadily decreasing Cu surface area in the case of **Cu@Ag$_{0.17}$** and **Cu@Ag$_{0.41}$** due to catalyst reconstruction. Namely, for those electrodes, the characteristic Cu(II)/Cu(I) reduction peaks appearing between 0.4 and 0.6 V$_{RHE}$ lost intensity faster relative to the Ag(I)/Ag(0) reduction peak upon potential cycling.

Composition-dependent Multicarbon Selectivity Exposed by Carbon Interfacing

In the specific case of CO$_2$ reduction over *sub*-10-nm spherical Cu NCs, inter-particle distance and packing density (*i.e.* loading)[74-76] are known to be crucial parameters for controlling CO$_2$RR selectivity. Therefore, we aimed at improving the initial spatial distribution of Cu-Ag NCs at the electrode surface by physically mixing nanoparticle suspensions with carbon black. The mixing procedure is outlined in **Figure 5a**, and representative overview SEM and HAADF-STEM images are shown in **Figure 5b-c**.
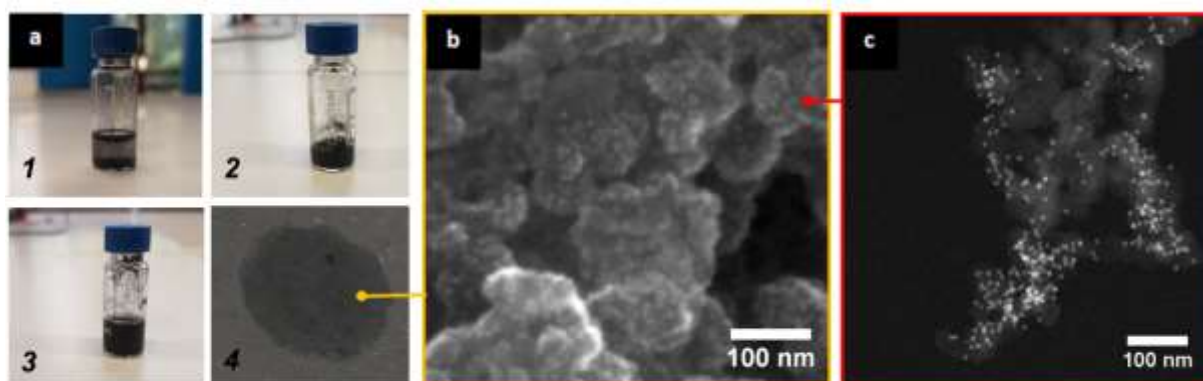
*Figure 5 (a) Outline of the dispersion procedure: (a1) mixing of C with a Cu-Ag suspension results in adsorption of the particles onto the surface of carbon black after which the Cu-Ag-supporting carbon sediments. (a2) slurry obtained after evaporation of hexane under inert conditions (a3) suspension after mild sonication in anhydrous 2-propanol without binder addition. (a4) drop-cast film on a gas diffusion electrode with a cross-section of ~1 cm². (b) SEM image of 11 wt.% **Cu/Ag$_{0.14}$/C** (c) HAADF-STEM image of **Cu@Ag$_{0.17}$** NCs on a carbon black nanoaggregate.*

Subsequent experiments were conducted in 0.1 M KHCO$_3$ rather than CsHCO$_3$ in order to assess the impact of cation and particle dispersion. **Figure 6a-b**, and in particular the

comparison between unsupported **Cu@Ag$_{0.17}$** in both electrolytes, demonstrates that catalyst dispersion had a stronger impact on selectivity.

Furthermore, a general trend emerged in which nanocrystals that were supported onto a carbon black carrier had a more pronounced C$_{2+}$ producing character compared to their unsupported counterparts. The densely packed carbon-supported Cu NCs (C/Cu ratio ~14, **Figure S.19**) produced ethylene as major CO$_2$RR product (30.5 %), while unsupported Cu NCs yielded mostly CO (39.8 %). Yet, the difference in measured overpotential was just 100 mV, -0.7 V$_{RHE}$ for unsupported Cu NCs and -0.8 V$_{RHE}$ for Cu NCs/C with post-electrolysis Cu loadings measuring ~30 µg cm^{-2} in both cases (see **Table S.3**). Dispersion on carbon black led thus to an increase in concentration of C$_{2+}$ products such as ethylene, ethanol, 1-propanol and acetate – ranked here in the order of decreasing selectivity (See also **Table S.4-S.5**) – which are characteristic products of CO$_2$RR over Cu-based electrodes under similar reaction conditions (**Table S.6**).[77-80]

Figure 6c zooms in on the major products formed at selected Cu-Ag/C electrodes and shows that in contrast to **Cu NCs/C**, the hydrogen evolution reaction is suppressed as the composition becomes richer in Ag. The excess charge available from suppression of HER is further accounted for by more pronounced carbon monoxide evolution and C$_2$ product formation, with a 87.7% total CO$_2$RR selectivity for **Cu@Ag$_{0.17}$/C** and a total C$_{2+}$ selectivity of ~50% for both **Cu/Ag$_{0.14}$/C** and **Cu@Ag$_{0.17}$/C**. In addition, it was observed that ethanol and acetate production were promoted at the expense of ethylene over Cu-Ag electrodes.
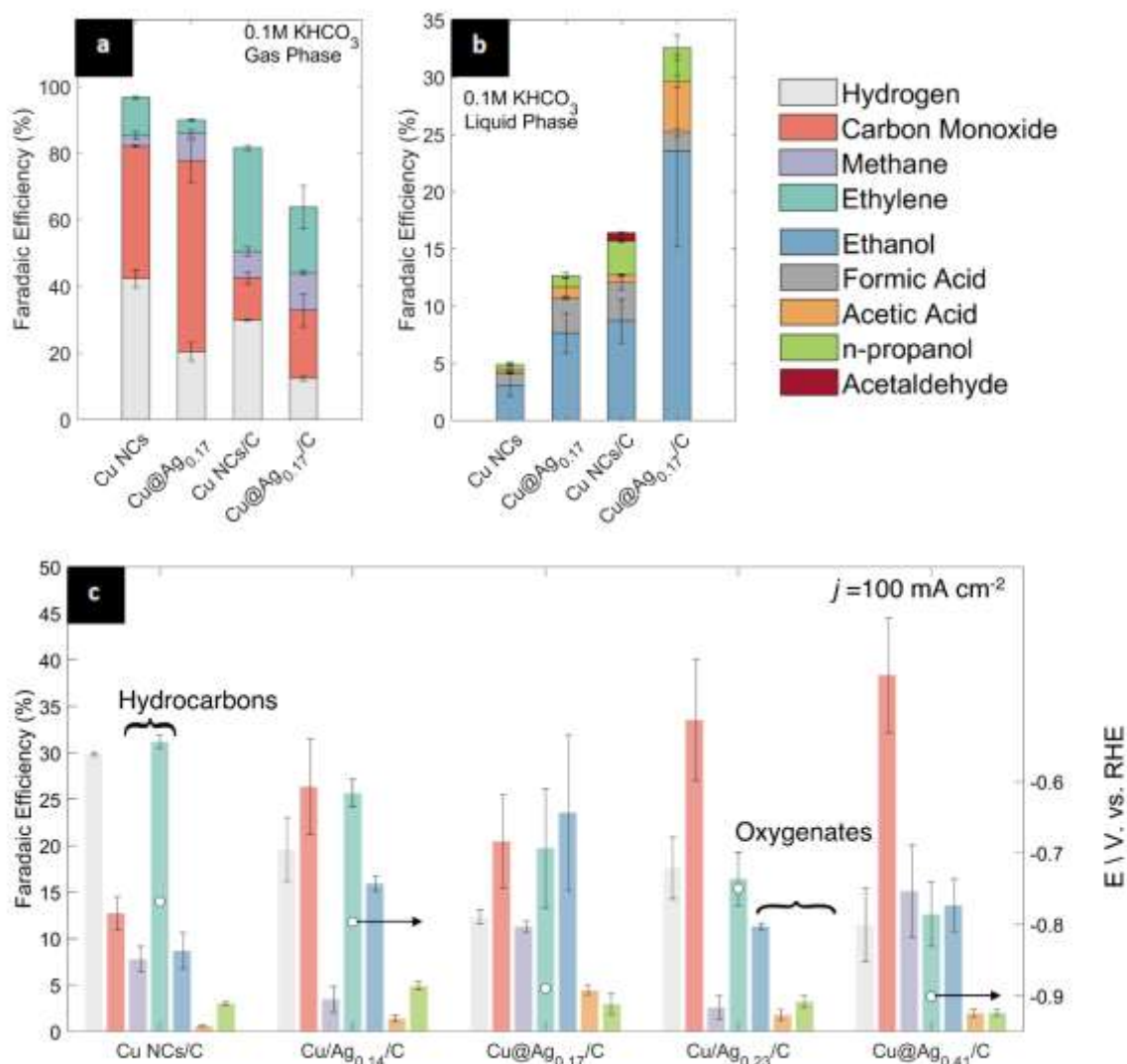
Figure 6 *(a) Gas phase Selectivity and (b) liquid phase selectivity of selected unsupported and carbon-supported Cu and Cu-Ag electrodes (c) Selectivity as a function of Ag at.% for Cu-Ag/C electrodes. Experiments were performed at 25°C in 0.1 M KHCO₃. A current density of 0.1 A cm⁻² was applied for a duration of 1 hour. Error bars give the standard deviation of two-three experiments, in which the gas phase was sampled four times over the course of 1 hour and the liquid phase was sampled once after electrolysis ended.*

Finally, **Figure 7** gives a comparison of SEM images taken from fresh Cu-Ag electrodes and Cu-Ag electrodes that were aged at 100 mA cm⁻² for a duration of 1 hour (example time-potential responses are given in **Figure S.20**). From inspection of those images, we arrived at the conclusion that polarization-induced reconstruction led to the formation of various particles on the scale of 10-100 nm. In aggregate, the dispersion in product distribution (10-30% of CO, ethylene and ethanol) seemed to be shaped primarily by the metal composition (which remained

unchanged after electrolysis, **Figure S.21**), electrode potential, and by the various reconstructed

Cu-Ag structures and interfaces appearing.
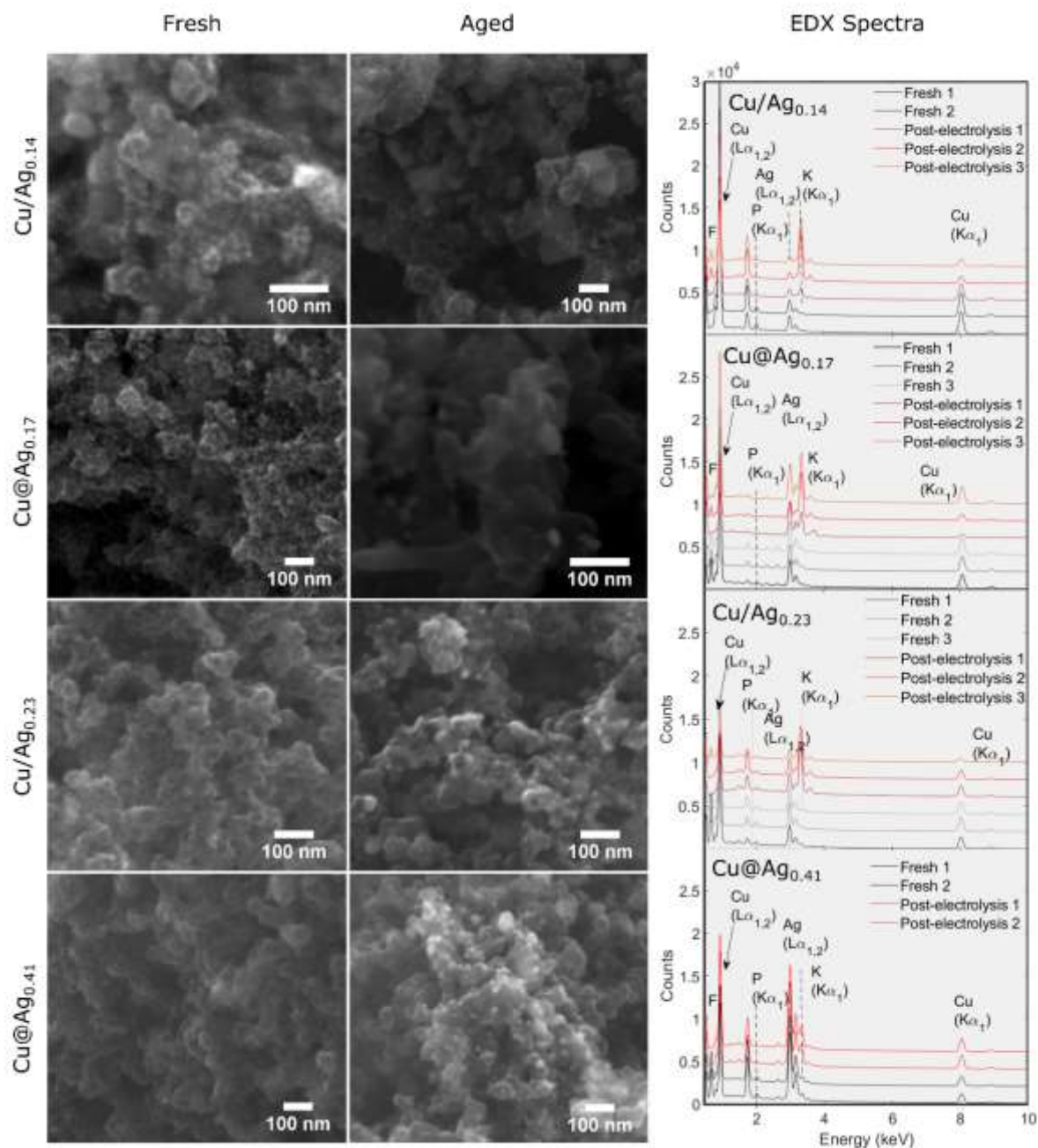
Figure 7 *SEM-EDX analysis of fresh and aged Cu-Ag electrodes (minimum of 1 hour at 0.1 A cm^{-2} in 0.1 M KHCO$_3$,) and corresponding EDX spectra (from 2-3 zones) showing pronounced peaks of Cu, Ag, P and F before electrolysis. Post-electrolysis samples are characterized by the additional presence of adsorbed K.*

Potential- and Composition-dependent Selectivity in Concentrated Bicarbonate Regime

Under the conditions employed in the previous section, ohmic drop and cell voltage increase rapidly with current density due to the low conductivity of the electrolyte. Therefore, and in order to probe the selectivity of the supported catalysts at rates > 0.1 A cm^{-2}, buffer strength (1 M KHCO$_3$, initial pH~8.1) and electrode area were increased (0.79 cm^2), resulting in lower area-specific resistance (~4 Ω cm^2 at 0.1 A cm^2).

In addition, analogues of Cu and Cu-Ag (15 and 22 at.% Ag) NCs were synthesized. As before, Cu-Ag NCs were characterized by means of HAADF-STEM (**Figure 8a1-b1**) and EDX (**Figure 8a2-b2**), showing that nanodimers (**Cu/Ag$_{0.15}$**) and core-shells (**Cu@Ag$_{0.22}$**) were formed (See also **Figure S.22** and **Table S.7**). Electrodes with targeted loadings in the range of 50-300 µg cm^{-2} were then prepared by using the physical mixing procedure outlined earlier, while keeping carbon black loading in the range of ~400 µg cm^{-2} (*i.e.* the C/Cu ratio was lowered to about 1.5-2). Linear Sweep Voltammetry (LSV) polarization curves recorded at 5 mV s^{-1} between -1.3V$_{RHE}$ and -0.4V$_{RHE}$ in CO$_2$-sat. 1M KHCO$_3$ showed that catalyst loading had a strong impact on the activity of **Cu@Ag$_{0.22}$/C**-based GDEs, especially between 150 and 300 µg cm^{-2} (**Figure S.23a**). Subsequent cycling of those electrodes under oxidative conditions exposed redox waves that are attributed to Cu^{2+}/Cu^{1+} and Ag$^+$/Ag transitions, with the magnitude of the former clearly increasing with loading (**Figure S.23b**).

Figure 8c shows a cross-sectional view combined with an EDX mapping of a **Cu@Ag$_{0.22}$/C**-coated GDE with a loading of about 195 µg$_{Cu}$ cm^{-2}, from which it can be estimated that the thickness of the Cu-Ag-rich carbon coating is roughly 10-15 microns. Moreover, the EDX mappings (see also **Figure S.24**) reveal the presence of fluorine (from the PTFE-treated GDE) and more importantly phosphorus (from the TDPA ligand) throughout the GDE. Since the concentration of TDPA scales with copper loading (P/Cu ratio = 0.04-0.06) its loading in the electrode may reach up to 50 µg cm^{-2}, which is a significant amount (*vide infra*). In order to

assess what might be the impact of such high loadings of both carbon black and TDPA we also prepared carbon-black-coated GDEs, as references for the support's activity, and (ligand- and carbon-black free) GDEs sputtered with Cu (40 ± 5 µg cm^{-2}), as benchmark for reactor performance (see **Table S.6**).

From the LSVs shown in **Figure S.25**, it is clear that the electrochemical activity of the carbon black-coated GDE is lower than that of the sputtered Cu reference and NCs-coated electrodes. Chronopotentiometry at 0.1 A cm^{-2} and -1.3 V_{RHE} indicated that the carbon black coated-GDE produces only hydrogen (~90-95%), carbon monoxide (5%), formate (2.7%) and traces of methane (0.4%). In contrast, product distributions obtained over Cu NCs at 0.1-0.3 A cm^{-2}, which are depicted in **Figure 8d1**, showed that formate (21%), ethylene (17%) and CO (17%) were the major products already at -1.0 V_{RHE}. The selectivity towards ethylene then increased at the expense of formate and carbon monoxide as a function of overpotential, reaching a maximum of 32.4% (96 mA cm^{-2}) at -1.26 V_{RHE}. At the same time, the selectivity towards ethanol amounted to 12.6% while that of hydrogen accounted for about 28% of the charge.

Figure 8d2 shows that **Cu/Ag$_{0.15}$/C** produced almost twice as much ethanol compared to Cu NCs at -1.0 V_{RHE} (6.4%), accompanied by a modest increase in CO selectivity and a decrease of formate selectivity. Ramping up the potential to -1.11 V_{RHE} cut the share of the unwanted side reactions to hydrogen and formate significantly, and led to formation of additional C_2 and C_3 products such as n-propanol, acetate and allyl alcohol. The gain in oxygenate production of **Cu/Ag$_{0.15}$/C** compared to the reference Cu NCs at 0.1 A cm^{-2} was admittedly low, only 30% in total. That surplus in selectivity was largely attributed to higher ethanol (+4.8 mA/cm^2) and acetate (+9.5 mA/cm^2) partial current densities. Despite the non-negligible contribution of HER from the carbon black support, the charge efficiency of **Cu/Ag$_{0.15}$/C** towards C_2-C_3 products reached a maximum of 47% at 0.3 A cm^{-2} (140.2 mA cm^{-2}) and ethanol and 1-propanol production rates peaked at 6.1 mg/h.cm^2 and 1.5 mg/h.cm^2, respectively. Accordingly, absolute

16

CO$_2$ turnovers reached about 0.03 mg CO$_2$ cm^{-2} s^{-1} and C$_2$-C$_3$ liquid product concentrations amounted to 0.05-0.1 wt.% (0.01 M ethanol) after just 20 minutes of electrolysis, due to the recycling of the electrolyte (which as a side-effect resulted in an increase of electrolyte pH with time, see **Table S.8**). Finally, **Cu@Ag$_{0.22}$/C** produced mainly carbon monoxide (22-25%) and a mix of ethylene (15-12%), ethanol (12%) and methane (7.5%-9%) between -1.09 V$_{RHE}$ and -1.16V$_{RHE.}$

Across the investigated series, hydrogen selectivity reached an average of 27.5% at -1.1 V$_{RHE}$. With the exception of Cu NCs, those values were higher compared to the 0.1 M KHCO$_3$ experiments described earlier, and higher compared to the values obtained over the reference sputtered Cu film. Taken together, those findings pointed towards several limiting contributions: first, the higher concentration of bicarbonate leads to additional promotion of HER due its role as local pH buffer[81-82] and proton donor.[83] Second, the elevated loading of TDPA, which accompanies any increase in catalyst loading or catalyst surface area (*e.g.* by decreasing particle size), may promote catalyst layer hydrophilicity and the HER as the ligand molecules abruptly desorb upon polarization (in the extreme case this leads to foaming, see also Supporting Video 1).

Despite that, the major catalytic trends - *i.e.* an increasing CO selectivity as a function of Ag at.% accompanied by a decrease in ethylene selectivity that was compensated by additional oxygenate production (notably of ethanol, acetate and allyl alcohol) - were again observed and therefore considered as intrinsic to the supported Cu-Ag NCs catalyst system, as will be discussed in more detail next.
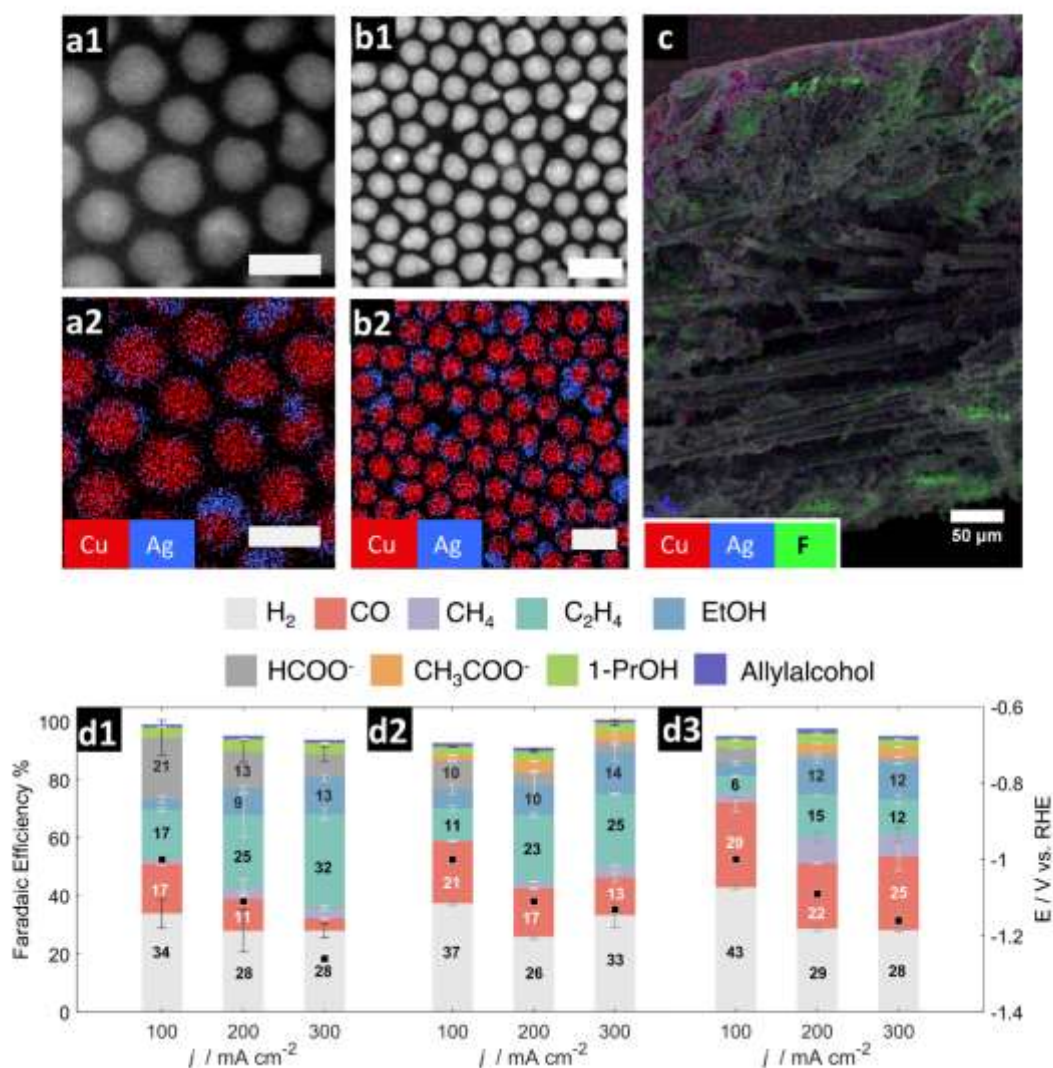
Figure 8 *HAADF-STEM and corresponding EDX maps of (a1-a2) **Cu/Ag₀.₁₅** , scale bar: 10 nm (b1-b2) **Cu@Ag₀.₂₂** , scale bar: 20 nm. Additional high-magnification HAADF-STEM images are provided in **Figure S.24**. (c) SEM-EDX cross-sectional mapping of a **Cu@Ag₀.₂₂/C** GDE, showing signal due to fluorine (F, green) and coinciding Cu(red) and Ag(blue) counts. Electron images and additional EDX mappings are provided in **Figure S.26**. (d1-d3) CO_2RR performance of **Cu NCs/C**, **Cu/Ag₀.₁₅/C** and **Cu@Ag₀.₂₂/C**, respectively. Experiments were performed in 1 M KHCO₃, 7.5 sccm CO₂, 0.25-2.5 cm³ cm⁻² min⁻¹catholyte flow in recycle mode, 25°C. Corresponding potential-time and pressure-time graphs are provided in the Supporting Information (**Figure S.26**).*

CO$_2$RR Pathways at Supported Cu-Ag/C electrodes

It is widely accepted that ethanol and acetate are formed by electrochemical reduction or disproportionation of acetaldehyde or its hydrolyzed form ethane-1,1-diol.[84] In contrast, allyl alcohol and 1-propanol probably originate from reduction of hydroxyacetone (although not observed in this work) and propionaldehyde (or their corresponding diols), with both disproportionation and hydrolysis reactions catalyzed by the highly alkaline conditions that are encountered locally at the solid-electrolyte interface.[85-86] Indeed, traces of acetaldehyde and propionaldehyde were detected in this work, but only in the outlet gas stream, where they became entrained due to their high volatility. In addition, ethanol was the major product among C$_2$ and C$_3$ oxygenates, whose formation was more pronounced over Cu-Ag nanocrystals. With respect to ethanol formation, it has been shown that both glyoxal and glycolaldehyde (of which trace amounts were detected) can reduce to acetaldehyde at an onset potential of -0.35 V$_{RHE}$, followed by ethanol forming at -0.6 V$_{RHE}$.[87] Later studies have demonstrated that the selectivity determining intermediate between ethanol and ethylene is likely *CH$_2$CHO, which is claimed to bond weakly through an oxygen atom to the surface of Cu and even weaker to Ag and Au.[88] In line with that notion, Clark *et al*[89] attributed the enhanced oxygenate production (particularly the formation of acetaldehyde) and suppression of HER of Cu-Ag surface alloys to reduced oxophilicity and H binding strength of surface Cu atoms, which are induced by compressive strain imposed by the larger neighboring Ag atoms. Cu-Ag surface alloys were later found to convert CO selectively to acetaldehyde at low overpotentials in basic media, and the product distribution shifted towards ethanol as the overpotential was ramped up.[90] Alternatively, Li *et al* calculated that doping Cu(111) with Ag increases the number of different binding sites 4-fold,[91] yielding Cu atoms in the vicinity of Ag with a lower affinity to carbon, rather than to oxygen, which was claimed to destabilize the ethylene pathway and thus to promote ethanol formation. Enhanced ethanol selectivity was also linked to a higher local *CO concentration

and to CO spillover from Ag ensembles to Cu ensembles.[92-93] Finally, two independent studies[94-95] have recently shown that the same spillover effect could be mimicked by feeding a 2% CO 98% CO_2 mixture to the catalyst instead of a pure CO_2 stream.

That interplay between (i) local electrolyte conditions, (ii) locally generated CO – superimposed by (iii) composition and morphology-dependent Cu-Ag nanocrystal reconstruction (this work) - is presented schematically in Figure 9.
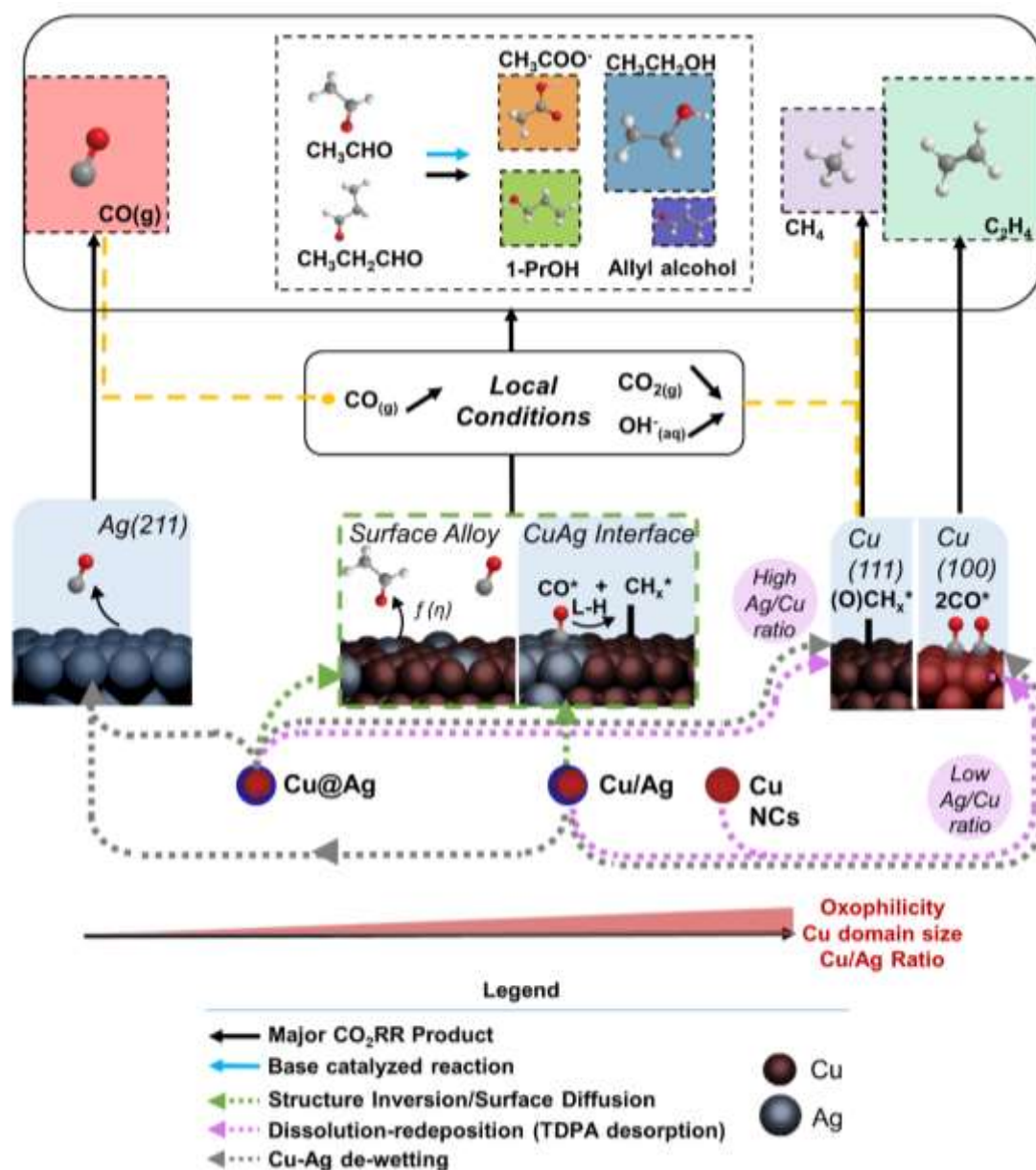
Figure 9 *Overview of reaction pathways and reconstruction pathways explaining the selectivity response observed in this work. Top: the major products observed. The size of the product boxes (color= legend Figure 8) reflects typical relative contribution to total selectivity. Center: Impact of local conditions - higher concentrations of locally generated OH⁻ ions and CO promote base catalyzed reactions and methane formation, respectively. Bottom: major catalyst reconstruction pathways leading to formation of polycrystalline Ag domains, Cu-Ag interfaces and polycrystalline Cu surfaces, depending in part on the NCs' initial morphology and the Ag/Cu atomic ratio.*

It is probable that a combination of those explanations may account for the selectivity of a complex catalyst such as supported Cu-Ag NCs, but nonetheless strong indications exist in favor of the CO spillover hypothesis and its underlying reaction mechanism. For instance, increasing the Ag/Cu ratio from zero (**Cu NCs/C**) to 0.7(**Cu@Ag$_{0.41}$**) can be regarded as an imaginary slider button that lowers the average binding energy of *CO in the entire system, resulting in increasing CO/C$_{2+}$ ratios (C$_{2+}$ includes ethylene, **Figure 10a**). Although this is accompanied by a decrease in hydrocarbon formation (the sum of methane and ethylene selectivity), the share of methane appears to grow at the expense of ethylene selectivity in the Cu-Ag series, as was shown in **Figure 6c**, with the exception of **Cu/Ag$_{0.23}$** (due in part to its lower electrode potential). Similar trends were also observed in 1 M KHCO$_3$ where at 200 mA cm^{-2} (-1.1 V$_{RHE}$) CO selectivity climbed from 11.0% (**Cu NCs/C**) to 17.0% (**Cu/Ag$_{0.15}$/C**) and further to 22.5% (**Cu@Ag$_{0.22}$/C**) and ethylene selectivity fell correspondingly from 25% to 23.0% down to 14.7%, respectively. At the same time, methane selectivity amounted to 3.9%, 2.5% and 7.5%, preserving the general increasing CO/C$_{2+}$ and decreasing hydrocarbon selectivity trends. The calculated totals and ratios obtained from those values are also plotted in **Figure 10**.

The 2-3-fold increase in total selectivity of Cu-Ag/C electrodes towards acetate and oxygenates compared to **Cu NCs/C** (see **Figure 10b, Table S.4**) leads ostensibly to an optimum in oxygenates/hydrocarbons ratio at moderate Ag concentrations (**Figure 10c, Table S.5**). Thus, a delicate balance exists between the rate at which CO is produced (controlled by Ag loading) and the rate at which it can be consumed at Cu-Ag or Cu domains. That rate is an intricate function of the crystals' domain size, exposed facets and kinetic regime, which in turn depends on the applied current density/potential and local pH.
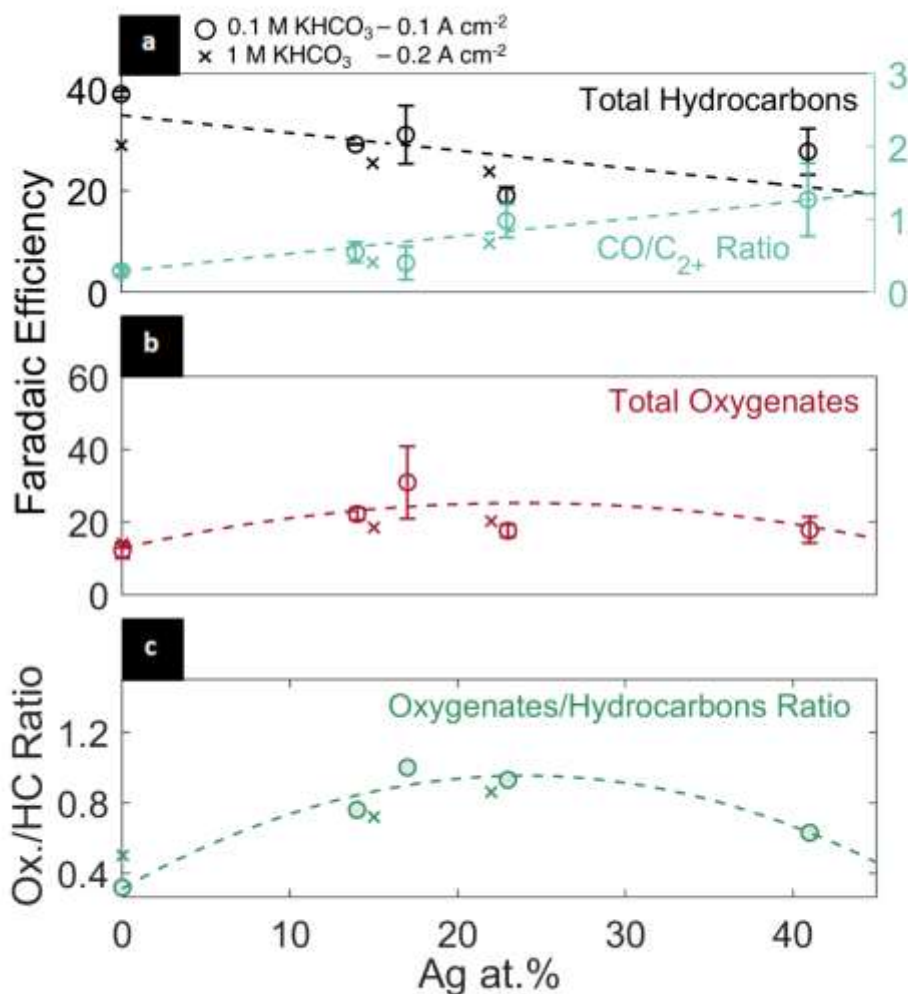
Figure 10 *(a) Total hydrocarbons faradaic efficiency and selectivity ratio between CO and C₂₊ formation as a function of formal Ag at.%, (b) total oxygenates faradaic efficiency as a function of formal Ag at.% and (c) the resulting Oxygenate/hydrocarbons ratio. Dashed lines to guide the eye.*

Interestingly, Ting *et al*[96] and Bounsanti *et al*[97] recently calculated that C-C coupling may proceed through a Langmuir-Hinshelwood-type *CH + *CO (*CO hydrogenation) pathway at Cu(111) surfaces adjacent to Ag clusters. Similar coupling mechanisms have been proposed earlier by Hori[98] for CO reduction on copper and Ren *et al*[99] for CO_2 reduction on electrodeposited Cu_xZn and Cu_xAg surfaces.

In line with those coupling mechanisms, the increasing average selectivity towards methane at -0.8-0.9 V_{RHE} in the series **Cu/Ag$_{0.14}$** - **Cu@Ag$_{0.17}$** - **Cu@Ag$_{0.41}$** indicates that relatively more Cu-bound *CHx species may convert further to methane as Cu composition and hence Cu core/domain size decrease, and with Cu and Ag adopting a more segregated configuration over time ("de-wetting"). Consequently, the transient increase in methane selectivity observed over the first hour of electrolysis at Cu-Ag electrodes is different from that observed over a 10-nm thick (6.9 µg$_{Cu}$ cm^{-2}) sputtered Cu layer benchmark (**Figure S.27**), where methane was found to be the major product (see **Table S.4**). In the case of the latter, the selectivity of methane and hydrogen rise simultaneously at the expense of CO, which indicates that polarization losses become more pronounced and thus that the kinetic overpotential at the cathode decreases with time, resulting in lower C_2 rates *versus* methane.[100] Methane and hydrogen formation increase over **Cu@Ag$_{0.17}$** (**Figure S.27**) in the course of the first hour as well, however, with the important exception that both CO and ethylene formation increase also with time, which indicates that globally speaking, the two metals are segregating into larger domains.

In contrast, the decoupling of selectivity between hydrogen and methane at Cu-Ag nanodimers in general, and **Cu/Ag$_{0.23}$/C** in particular, points out at favorable Cu-Ag interactions due to a steadily growing fractional coverage of CO, θ(CO), generated by Ag, and CO reduction/coupling over relatively large Cu domains or Cu-Ag interfaces. Since, according to the mechanism proposed by Hori *et al*[98] for CO reduction over Cu, the rate of methane evolution is proportional to θ(CO), we can expect methane selectivity to change both as a function of time and as a function of Ag content, in agreement with the experimental data.

CONCLUSIONS

We have investigated a modified synthetic pathway for the formation of electrocatalytic TDPA-capped Cu-Ag NCs by exploring the use of Cu(II) acetate monohydrate and near stoichiometric ligand-to-copper (P/Cu) ratios. High-resolution electron microscopy and spectroscopy proved that *sub*-10-nm Cu@Ag core-shells and Cu/Ag nanodimers could be obtained after one or two galvanic replacement steps depending on the diameter of the Cu NC precursor.

A protocol for dispersing the nanocrystals on carbon black at high packing densities, which was outlined here in detail, facilitated considerably the mapping of the composition-selectivity relationship in the range of Ag atomic percentages between 14 and 41 at.%. Consequently, CO_2RR selectivity shifted from ethylene formation to ethanol between Cu NCs/C and Cu-Ag/C based electrodes, accompanied by suppression of the HER, higher CO/C_{2+} ratios and a two-threefold increase of the oxygenate-to-hydrocarbon ratio at moderate Ag at.%. With that, the total C_2-C_3 selectivity of **Cu/Ag$_{0.14}$/C** nanodimers and **Cu@Ag$_{0.17}$/C** core-shells amounted to 50% at neutral bulk pH and 0.1 A cm^{-2}.

Using higher catalyst loadings of 200-300 µg$_{Cu}$ cm^{-2}, we achieved current densities of 0.2-0.3 A cm^{-2} at -1.0-1.2 V_{RHE} in 1 M $KHCO_3$, with C_2-C_3 charge efficiency reaching a maximum of 47% (140 mA cm^{-2}) for **Cu/Ag$_{0.15}$/C**. By recycling the electrolyte, the combined concentration of ethanol, n-propanol and allyl alcohol in the liquid phase surpassed 0.05 wt.%, albeit with a significant increase in electrolyte pH and build-up of carbonate, which in the long run hampers electrode stability and promotes the HER. Overall, the catalytic trends observed at those high CO_2RR rates pointed out towards a marked influence of local CO concentration and CO-spillover.

To conclude, our findings underscore the importance of two emerging fields in ligand and reaction interface/reactor engineering. Integration of *sub*-10-nm Cu-Ag nanocrystals into more advanced carbon-based CO_2 reduction interfaces – where changes in the electronic properties

of the support/ligand may drive changes in HER selectivity, local CO_2/CO balance, and hydrophobicity – could enable further optimization of the NCs' dynamic behavior for the production and accumulation of multicarbon products.

METHODS

Materials Copper(II) acetate monohydrate (p.a., Janssen Chimica), Trioctylamine (97%, Acros Organics), Ethanol (99.5% Extra Dry, AcrosSeal®, Acros Organics), 2-propanol (99.5%, Extra Dry over Molecular Sieve, AcrosSeal® Acros Organics), Tetradecylphosphonic acid (98%, Sigma Aldrich), Isoamyl ether (99%, Sigma Aldrich), silver trifluoroacetate (99.99%, trace metal basis, Sigma Aldrich), cesium bicarbonate (99.99%, trace metal basis, Sigma Aldrich), potassium bicarbonate (99.99%, trace metal basis, Sigma Aldrich), Sigracet® 39BC (SGL Carbon), ENSACO®-350G (Imerys Graphite and Carbon).

Synthesis Polycrystalline Cu NCs were synthesized using the thermal decomposition of copper(II) acetate monohydrate in trioctylamine, a modified version of literature procedures that employ Cu(I)acetate as precursor. [101-102] Cu-Ag NCs were synthesized by galvanic exchange of Cu(0) with Ag-trifluoroacetate (Ag-TFA) in isoamyl ether at room temperature.[55-56] Detailed procedures are given in the Supporting Information.

UV-Vis spectra were recorded using a Hitachi U-2001 apparatus in the interval 300-800 nm. Cu and Cu-Ag suspensions were diluted 100-200 fold in hexane.

ICP-MS The bulk concentrations of Cu and Ag were quantified using an Agilent 7500 Series Inductively Coupled Plasma Mass Spectrometer (ICP-MS). A 100µl aliquot was digested in *aqua regia* or nitric acid at 70°C overnight. To determine catalyst loadings, a 0.28 cm^2 disk of a coated gas diffusion electrode taken from fresh and aged electrodes was subjected to digestion overnight. Both solutions were then diluted to the appropriate concentration range (100-300 ppb) and analyzed.

X-ray Photoelectron Spectroscopy (XPS) measurements were performed with a Physical Electronics PHI VersaProbe II system using an Al Kα (1486.6 eV) monochromatic X-ray source. The system was equipped with an automatic electron neutralizer and measured across an area 100 µm in diameter. High-resolution scans were recorded with a pass energy of 26.5 eV and a step size of 0.1 eV. Spectra were charge-compensated by setting the graphitic C1s band to 284.8 eV. The area and full width at half maximum of the Cu $2p_{3/2}$ and Ag $3d_{5/2}$ lines were calculated using the PHI MultiPak software (V8.0) by fitting a Gaussian-Laurentzian line shape to the peak with a Shirley background. Elemental compositions were then calculated using internal relative sensitivity factors in the PHI MultiPak software and validated using the following relationship:

$$x_{Cu} = \frac{I_{Cu2p,exptl}/R_0}{(I_{Cu2p,exptl}/R_0 + I_{Ag3d,exptl})}$$

Where $I_{Cu2p,exptl}$ and $I_{Ag3d,exptl}$ are the measured intensities of the Cu $2p_{3/2}$ and Ag $3d_{5/2}$ lines from the surface of drop-cast Cu-Ag films, and R_0 is the intensity ratio of the $2p_{3/2}$ line of pure metallic Cu to the $3d_{5/2}$ of pure metallic silver.

Cu-Ag suspensions were briefly exposed to air, drop-cast on a glass microscope slide and then quickly transferred to the pre vacuum chamber of the XPS device.

Electron Microscopy Scanning electron microscopy measurements were performed on a Thermo Fischer Scientific Quanta FEG 250 microscope, operated at an acceleration voltage of 15kV. Samples suitable for High Angle Annular Dark Field Scanning Transmission Electron Microscopy (HAADF-STEM) were prepared in the glovebox under Ar atmosphere, by drop casting the sample solution onto ultrathin-film (UTF) Au TEM grids. For high-resolution imaging, the TEM grids were washed in a mixture of activated carbon and ethanol following the method by Chen *et al*[103] to remove excess ligands and decrease contamination during electron microscopy investigation. HAADF-STEM images and STEM Energy Dispersive X-ray Spectroscopy (STEM–EDX) maps were acquired using an aberration corrected Thermo Fischer Scientific Titan electron microscope operated at 300kV and a Thermo Fischer Scientific Osiris electron microscope operated at 200kV and both equipped with the ChemiSTEM system.[104]

Projected nanocrystal cross-sections (A) were extracted from HAADF-STEM images using the MorphoLibJ plugin[105] in ImageJ (V1.52a). Particle diameters were then calculated as $d=2(A/\pi)^{1/2}$ to construct histograms of particle size distributions.

Electrochemistry Electrochemical measurements were performed using an Autolab M204 potentiostat (Metrohm). Chronopotetiometric electrolysis experiments were conducted in a gas-fed hybrid flow-cell with a recycled catholyte stream (0.2-2 ml/min). The CO_2 (99.996%, Nippon Gases) flow rate entering the channel was between 5-7.5 sccm by a mass flow controller (GF-080, Brooks Instruments). The backpressure in the gas channel was measured by a Gefran TK-series pressure sensor with an accuracy of ±2.5 mbar and range of 0-1 barg. Pressure readings were logged using an I/O device (National instruments, NI6000) which was interfaced with MATLAB® R2016a for data recording. A 1 mm Ag/AgCl leak-free electrode (W3-690053, Harvard Apparatus) was used as reference in the cell. Catholyte and Anolyte were separated by a Selemion® DSVN anion exchange membrane (AGC Engineering Co., Japan). Catholyte pH was measured using a 'Leak Free' 1 mm pH probe (AMANI 1000L, Harvard Apparatus). On the anode side, a carbon cloth was used as counter electrode with conductive Al foil as current collector. The uncompensated resistance R_u and the resulting ohmic drop IR_u were determined using current interrupt and electrochemical impedance spectroscopy. All potentials are reported *versus* the reversible hydrogen electrode (RHE), unless stated otherwise, and according to the following conversion:

$$E_{RHE} = E_{vs.\ ref} + 0.210V + 0.059 \cdot pH + IR_u$$

Selectivity was calculated using the expression:

$$FE_i = \frac{n_i z_i F}{Q}$$

Where n_i is the amount of product generated (in moles), z_i is the number of electrons transferred per mole product, F Faraday's constant 96485 C mol e$^-$ and Q the charge transferred (in coulombs).

Electrode Preparation Working electrodes (diameter 1 inch) were prepared by drop casting particles directly from an NCs suspension in hexane onto gas diffusion electrodes (Sigracet 39BC, SGL Carbon). Alternatively, a given volume of particle suspension was mixed with carbon black (ENSACO®, Imerys Carbon) under inert atmosphere to achieve a C/Cu ratio of 2 (1 M experiments)-14 (0.1 M experiments) and electrode carbon loadings of ~0.35-0.4 mg cm^{-2}. The suspension was sonicated under argon atmosphere, vortexed (for low C/Cu ratios) and left to sediment for several minutes after which the hexane was removed by evaporation. An identical volume of anhydrous 2-propanol was then used to re-disperse the particles. The ink was then sonicated prior to drop casting (0.1 M experiments) or airbrushing (1 M experiments). Total metal loadings were in the range of 25-300 µg cm^{-2} depending on the processing conditions (See also **Table S.3 and Table S.7**). The ligand- and carbon-black free Cu film benchmarks were prepared by sputtering 10 nm or 70 nm layers of Cu onto gas diffusion electrodes using Cu targets (99.9%, EM-Tec, Micro-to-Nano) and a Leica EM ACE600 apparatus.

Gaseous and Liquid Product analysis Gaseous products were separated using a micropacked column (ShinCarbon ST 100/120, 2 m, 1 mm ID, Restek) with He as carrier gas and detected by means of a thermal conductivity detector (TCD) operating at 200°C. Samples were injected automatically into the column from the reactor's outlet. Liquid products dissolved in the catholyte and to a lesser extent in the anolyte streams were quantified by means of high-performance liquid chromatography (HPLC) and GC equipped with a Flame Ionization Detector (FID). More details are provided in the Supporting Information.

AUTHOR INFORMATION

Corresponding Authors

Daniel.Choukroun@uantwerpen.be, Tom.Breugelmans@uantwerpen.be

Author Contributions

D.C. - manuscript, synthesis, SEM, cell design and fabrication, electrochemical measurements, data analysis **L.P.** – synthesis, cyclic voltammetry, **C.L. S.H., and S.A.** - TEM, **K.B. and T.H**. – XPS. **S.B.** and **T.B.** supervised the project.

ASSOCIATED CONTENT

Supporting Information

Appearance of Cu and Cu-Ag NCs suspensions (Figures S.1 and S.2) and their optical response (S.3); HAADF-STEM image of Cu NCs prepared with P/Cu ratio of 0.1 (S.4); Simplified synthetic scheme (S.5); Overview HAADF-STEM image and histograms of Cu-Ag NCs (S.6-S.9); XPS spectra, Cu LMM spectra and deconvolution (S.10-S.12); STEM-EDX mapping of Cu@Ag$_{0.54}$ (S.13); Schematic representation of the employed electrochemical cell (S.14); Analysis of multicarbon products (S.15-S.16); Cyclic voltammograms of Cu-Ag NCs (S.17-S.18); SEM-EDX analysis of Cu NCs/C (S.19); t-E data (S.20) and quantitative EDX analysis (S.21) of supported Cu-Ag electrodes; HAADF-STEM images of Cu/Ag$_{0.15}$ and Cu@Ag$_{0.22}$ (S.22); LSVs, CVs (S.23) and SEM-EDX cross-section (S.24) of Cu@Ag$_{0.22}$/C; Comparison of LSVs (S.25), E-t and p-t data (S.26) in 1M KHCO$_3$; Analysis of transient gas evolution (S.27); Summary of XPS analysis (Table S.1); Electrode properties, summary and review of electrochemical performance (Table S.2-S.8); List of products and their analytical detection limits (Tables S.9-S.10) (PDF)

Video (with audio) showing TDPA desorption and foaming after polarization (MP4)

ACKNOWLEDGEMENT

REFERENCES

1. Gurudayal; Bullock, J.; Srankó, D. F.; Towle, C. M.; Lum, Y.; Hettick, M.; Scott, M. C.; Javey, A.; Ager, J., Efficient Solar-Driven Electrochemical CO2 Reduction to Hydrocarbons and Oxygenates. *Energy Environ. Sci.* **2017**, *10*, 2222-2230.
2. Bushuyev, O. S.; De Luna, P.; Dinh, C. T.; Tao, L.; Saur, G.; van de Lagemaat, J.; Kelley, S. O.; Sargent, E. H., What Should We Make with CO2 and How Can We Make It? *Joule* **2018**, *2*, 825-832.
3. Obama, B., The Irreversible Momentum of Clean Energy. *Science* **2017**, *355*, 126.
4. De Arquer, F. P. G.; Dinh, C.-T.; Ozden, A.; Wicks, J.; McCallum, C.; Kirmani, A. R.; Nam, D.-H.; Gabardo, C.; Seifitokaldani, A.; Wang, X., CO2 Electrolysis to Multicarbon Products at Activities Greater than 1 A cm− 2. *Science* **2020**, *367*, 661-666.
5. Smith, W. A.; Burdyny, T.; Vermaas, D. A.; Geerlings, H., Pathways to Industrial-Scale Fuel Out of Thin Air from CO2 Electrolysis. *Joule* **2019**, *3*, 1822-1834.
6. De Luna, P.; Hahn, C.; Higgins, D.; Jaffer, S. A.; Jaramillo, T. F.; Sargent, E. H., What Would It Take for Renewably Powered Electrosynthesis to Displace Petrochemical Processes? *Science* **2019**, *364*, eaav3506.
7. Hahn, C.; Hatsukade, T.; Kim, Y.-G.; Vailionis, A.; Baricuatro, J. H.; Higgins, D. C.; Nitopi, S. A.; Soriaga, M. P.; Jaramillo, T. F., Engineering Cu Surfaces for the Electrocatalytic Conversion of CO2: Controlling Selectivity toward Oxygenates and Hydrocarbons. *Proc. Natl. Acad. Sci. U. S. A.* **2017**, *114*, 5918-5923.
8. Ross, M. B.; De Luna, P.; Li, Y.; Dinh, C.-T.; Kim, D.; Yang, P.; Sargent, E. H., Designing Materials for Electrochemical Carbon Dioxide Recycling. *Nat. Catal.* **2019**, *2*, 648-658.
9. Todorova, T. K.; Schreiber, M. W.; Fontecave, M., Mechanistic Understanding of CO2 Reduction Reaction (CO2RR) toward Multicarbon Products by Heterogeneous Copper-Based Catalysts. *ACS Catal.* **2020**, *10*, 1754-1768.
10. Zheng, Y.; Vasileff, A.; Zhou, X.; Jiao, Y.; Jaroniec, M.; Qiao, S.-Z., Understanding the Roadmap for Electrochemical Reduction of CO2 to Multi-Carbon Oxygenates and Hydrocarbons on Copper-Based Catalysts. *J. Am. Chem. Soc.* **2019**, *141*, 7646-7659.
11. Vasileff, A.; Xu, C. C.; Jiao, Y.; Zheng, Y.; Qiao, S. Z., Surface and Interface Engineering in Copper-Based Bimetallic Materials for Selective CO2 Electroreduction. *Chem* **2018**, *4*, 1809-1831.
12. Zhuang, T. T.; Pang, Y. J.; Liang, Z. Q.; Wang, Z. Y.; Li, Y.; Tan, C. S.; Li, J.; Dinh, C. T.; De Luna, P.; Hsieh, P. L.; Burdyny, T.; Li, H. H.; Liu, M. X.; Wang, Y. H.; Li, F. W.; Proppe, A.; Johnston, A.; Nam, D. H.; Wu, Z. Y.; Zheng, Y. R.*, et al.*, Copper Nanocavities Confine Intermediates for Efficient Electrosynthesis of C3 Alcohol Fuels from Carbon Monoxide. *Nat. Catal.* **2018**, *1*, 946-951.
13. Burdyny, T.; Graham, P. J.; Pang, Y.; Dinh, C.-T.; Liu, M.; Sargent, E. H.; Sinton, D., Nanomorphology-Enhanced Gas-Evolution Intensifies CO2 Reduction Electrochemistry. *ACS Sustainable Chem. Eng.* **2017**, *5*, 4031-4040.
14. Arán-Ais, R. M.; Gao, D.; Roldan Cuenya, B., Structure- and Electrolyte-Sensitivity in CO2 Electroreduction. *Acc. Chem. Res.* **2018**, *51*, 2906-2917.

15.	Ma, W.; Xie, S.; Liu, T.; Fan, Q.; Ye, J.; Sun, F.; Jiang, Z.; Zhang, Q.; Cheng, J.; Wang, Y., Electrocatalytic Reduction of CO2 to Ethylene and Ethanol through Hydrogen-Assisted C–C Coupling over Fluorine-Modified Copper. *Nat. Catal.* **2020**, *3*, 478-487.

16.	Xu, H.; Rebollar, D.; He, H.; Chong, L.; Liu, Y.; Liu, C.; Sun, C.-J.; Li, T.; Muntean, J. V.; Winans, R. E.; Liu, D.-J.; Xu, T., Highly Selective Electrocatalytic CO2 Reduction to Ethanol by Metallic Clusters Dynamically Formed from Atomically Dispersed Copper. *Nat. Energy* **2020**, *5*, 623-632.

17.	Lee, C. W.; Yang, K. D.; Nam, D. H.; Jang, J. H.; Cho, N. H.; Im, S. W.; Nam, K. T., Defining a Materials Database for the Design of Copper Binary Alloy Catalysts for Electrochemical CO2 Conversion. *Adv. Mater.* **2018**, *30*, 18.

18.	Kim, D.; Resasco, J.; Yu, Y.; Asiri, A. M.; Yang, P., Synergistic Geometric and Electronic Effects for Electrochemical Reduction of Carbon Dioxide Using Gold–Copper Bimetallic Nanoparticles. *Nat. Commun.* **2014**, *5*, 4948.

19.	Wang, P.; Yang, H.; Xu, Y.; Huang, X.; Wang, J.; Zhong, M.; Cheng, T.; Shao, Q., Synergized Cu/Pb Core/Shell Electrocatalyst for High-Efficiency CO2 Reduction to C2+ Liquids. *ACS Nano* **2021**, *15*, 1039-1047.

20.	Lyengar, P.; Huang, J. F.; De Gregorio, G. L.; Gadiyar, C.; Buonsanti, R., Size Dependent Selectivity of Cu Nano-Octahedra Catalysts for the Electrochemical Reduction of CO2 to CH4. *Chem. Commun.* **2019**, *55*, 8796-8799.

21.	Reske, R.; Mistry, H.; Behafarid, F.; Roldan Cuenya, B.; Strasser, P., Particle Size Effects in the Catalytic Electroreduction of CO2 on Cu Nanoparticles. *J. Am. Chem. Soc.* **2014**, *136*, 6978-6986.

22.	De Gregorio, G. L.; Burdyny, T.; Loiudice, A.; Iyengar, P.; Smith, W. A.; Buonsanti, R., Facet-Dependent Selectivity of Cu Catalysts in Electrochemical CO2 Reduction at Commercially Viable Current Densities. *ACS Catal.* **2020**, *10*, 4854-4862.

23.	Nitopi, S.; Bertheussen, E.; Scott, S. B.; Liu, X.; Engstfeld, A. K.; Horch, S.; Seger, B.; Stephens, I. E. L.; Chan, K.; Hahn, C.; Nørskov, J. K.; Jaramillo, T. F.; Chorkendorff, I., Progress and Perspectives of Electrochemical CO2 Reduction on Copper in Aqueous Electrolyte. *Chem. Rev.* **2019**, *119*, 7610-7672.

24.	Garza, A. J.; Bell, A. T.; Head-Gordon, M., Mechanism of CO2 Reduction at Copper Surfaces: Pathways to C2 Products. *ACS Catal.* **2018**, *8*, 1490-1499.

25.	Ledezma-Yanez, I.; Gallent, E. P.; Koper, M. T. M.; Calle-Vallejo, F., Structure-Sensitive Electroreduction of Acetaldehyde to Ethanol on Copper and Its Mechanistic Implications for CO and CO2 Reduction. *Catal. Today* **2016**, *262*, 90-94.

26.	Birdja, Y. Y.; Pérez-Gallent, E.; Figueiredo, M. C.; Göttle, A. J.; Calle-Vallejo, F.; Koper, M. T. M., Advances and Challenges in Understanding the Electrocatalytic Conversion of Carbon Dioxide to Fuels. *Nat. Energy* **2019**, *4*, 732-745.

27.	Higgins, D.; Landersp, A. T.; Ji, Y. F.; Nitopi, S.; Morales-Guio, C. G.; Wang, L.; Chan, K. R.; Hahn, C.; Jaramillo, T. F., Guiding Electrochemical Carbon Dioxide Reduction toward Carbonyls Using Copper Silver Thin Films with Interphase Miscibility. *ACS Energy Lett.* **2018**, *3*, 2947-2955.

28.	Hoang, T. T. H.; Ma, S.; Gold, J. I.; Kenis, P. J. A.; Gewirth, A. A., Nanoporous Copper Films by Additive-Controlled Electrodeposition: CO2 Reduction Catalysis. *ACS Catal.* **2017**, *7*, 3313-3321.

29.	Martić, N.; Reller, C.; Macauley, C.; Löffler, M.; Reichert, A. M.; Reichbauer, T.; Vetter, K.-M.; Schmid, B.; McLaughlin, D.; Leidinger, P.; Reinisch, D.; Vogl, C.; Mayrhofer, K. J. J.; Katsounaros, I.; Schmid, G., Ag2Cu2O3 – A Catalyst Template Material for Selective Electroreduction of CO to C2+ Products. *Energy Environ. Sci.* **2020**, *13*, 2993-3006.

30.	Lee, S.; Park, G.; Lee, J., Importance of Ag-Cu Biphasic Boundaries for Selective Electrochemical Reduction of CO2 to Ethanol. *ACS Catal.* **2017**, *7*, 8594-8604.

31.	Dutta, A.; Montiel, I. Z.; Erni, R.; Kiran, K.; Rahaman, M.; Drnec, J.; Broekmann, P., Activation of Bimetallic AgCu Foam Electrocatalysts for Ethanol Formation from CO2 by Selective Cu Oxidation/Reduction. *Nano Energy* **2020**, *68*, 104331.

32.	Lv, X.; Shang, L.; Zhou, S.; Li, S.; Wang, Y.; Wang, Z.; Sham, T.-K.; Peng, C.; Zheng, G., Electron-Deficient Cu Sites on Cu3Ag1 Catalyst Promoting CO2 Electroreduction to Alcohols. *Adv. Energy Mater.* **2020**, *10*, 2001987.

33.   Lequien, F.; Creuze, J.; Berthier, F.; Braems, I.; Legrand, B., Superficial Segregation, Wetting, and Dynamical Equilibrium in Bimetallic Clusters: A Monte Carlo Study. *Phys. Rev. B* **2008**, *78*, 075414.

34.   Lee, C.; Kim, N. R.; Koo, J.; Lee, Y. J.; Lee, H. M., Cu-Ag Core–Shell Nanoparticles with Enhanced Oxidation Stability for Printed Electronics. *Nanotechnology* **2015**, *26*, 455601.

35.   Zhu, X.; Rong, H.; Zhang, X.; Di, Q.; Shang, H.; Bai, B.; Liu, J.; Liu, J.; Xu, M.; Chen, W.; Zhang, J., Compressive Surface Strained Atomic-Layer Cu2O on Cu@Ag Nanoparticles. *Nano Res.* **2019**, *12*, 1187-1192.

36.   Manna, L.; Scher, E. C.; Alivisatos, A. P., Synthesis of Soluble and Processable Rod-, Arrow-, Teardrop-, and Tetrapod-Shaped CdSe Nanocrystals. *J. Am. Chem. Soc.* **2000**, *122*, 12700-12706.

37.   Mokari, T.; Zhang, M.; Yang, P., Shape, Size, and Assembly Control of PbTe Nanocrystals. *J. Am. Chem. Soc.* **2007**, *129*, 9864-9865.

38.   Glaria, A.; Cure, J.; Piettre, K.; Coppel, Y.; Turrin, C.-O.; Chaudret, B.; Fau, P., Deciphering Ligands' Interaction with Cu and Cu2O Nanocrystal Surfaces by NMR Solution Tools. *Chem. - Eur. J.* **2015**, *21*, 1169-1178.

39.   Li, Q.; Fu, J.; Zhu, W.; Chen, Z.; Shen, B.; Wu, L.; Xi, Z.; Wang, T.; Lu, G.; Zhu, J.-j.; Sun, S., Tuning Sn-Catalysis for Electrochemical Reduction of CO2 to CO *via* the Core/Shell Cu/SnO2 Structure. *J. Am. Chem. Soc.* **2017**, *139*, 4290-4293.

40.   Huang, J. F.; Buonsanti, R., Colloidal Nanocrystals as Heterogeneous Catalysts for Electrochemical CO2 Conversions. *Chem. Mater.* **2019**, *31*, 13-25.

41.   Wang, Y.; Wang, D. G.; Dares, C. J.; Marquard, S. L.; Sheridan, M. V.; Meyer, T. J., CO2 Reduction to Acetate in Mixtures of Ultrasmall (Cu)(n),(Ag)(m) Bimetallic Nanoparticles. *Proc. Natl. Acad. Sci. U. S. A.* **2018**, *115*, 278-283.

42.   Chang, Z.; Huo, S.; Zhang, W.; Fang, J.; Wang, H., The Tunable and Highly Selective Reduction Products on Ag@Cu Bimetallic Catalysts toward CO2 Electrochemical Reduction Reaction. *J. Phys. Chem. C* **2017**, *121*, 11368-11379.

43.   Yang, C.; Ko, B. H.; Hwang, S.; Liu, Z.; Yao, Y.; Luc, W.; Cui, M.; Malkani, A. S.; Li, T.; Wang, X., Overcoming Immiscibility toward Bimetallic Catalyst Library. *Sci. Adv.* **2020**, *6*, eaaz6844.

44.   Choukroun, D.; Daems, N.; Kenis, T.; Van Everbroeck, T.; Hereijgers, J.; Altantzis, T.; Bals, S.; Cool, P.; Breugelmans, T., Bifunctional Nickel–Nitrogen-Doped-Carbon-Supported Copper Electrocatalyst for CO2 Reduction. *The Journal of Physical Chemistry C* **2020**.

45.   Wang, X.; Wang, Z.; García de Arquer, F. P.; Dinh, C.-T.; Ozden, A.; Li, Y. C.; Nam, D.-H.; Li, J.; Liu, Y.-S.; Wicks, J.; Chen, Z.; Chi, M.; Chen, B.; Wang, Y.; Tam, J.; Howe, J. Y.; Proppe, A.; Todorović, P.; Li, F.; Zhuang, T.-T., *et al.*, Efficient Electrically Powered CO2-to-Ethanol *via* Suppression of Deoxygenation. *Nat. Energy* **2020**, *5*, 478-486.

46.   Tan, Y. C.; Lee, K. B.; Song, H.; Oh, J., Modulating Local CO2 Concentration as a General Strategy for Enhancing C−C Coupling in CO2 Electroreduction. *Joule* **2020**, *4*, 1104-1120.

47.   Wang, H.; Tzeng, Y.-K.; Ji, Y.; Li, Y.; Li, J.; Zheng, X.; Yang, A.; Liu, Y.; Gong, Y.; Cai, L.; Li, Y.; Zhang, X.; Chen, W.; Liu, B.; Lu, H.; Melosh, N. A.; Shen, Z.-X.; Chan, K.; Tan, T.; Chu, S., *et al.*, Synergistic Enhancement of Electrocatalytic CO2 Reduction to C2 Oxygenates at Nitrogen-Doped Nanodiamonds/Cu Interface. *Nat. Nanotechnol.* **2020**, *15*, 131-137.

48.   Kuang, S.; Li, M.; Xia, R.; Xing, L.; Su, Y.; Fan, Q.; Liu, J.; Hensen, E. J. M.; Ma, X.; Zhang, S., Stable Surface-Anchored Cu Nanocubes for CO2 Electroreduction to Ethylene. *ACS Appl. Nano Mater.* **2020**, *3*, 8328-8334.

49.   Manthiram, K.; Beberwyck, B. J.; Alivisatos, A. P., Enhanced Electrochemical Methanation of Carbon Dioxide with a Dispersible Nanoscale Copper Catalyst. *J. Am. Chem. Soc.* **2014**, *136*, 13319-13325.

50.   Pankhurst, J. R.; Iyengar, P.; Loiudice, A.; Mensi, M.; Buonsanti, R., Metal–Ligand Bond Strength Determines the Fate of Organic Ligands on the Catalyst Surface during the Electrochemical CO2 Reduction Reaction. *Chem. Sci.* **2020**, *11*, 9296-9302.

51.   Qiu, Y. L.; Zhong, H. X.; Xu, W. B.; Zhang, T. T.; Li, X. F.; Zhang, H. M., Tuning the Electrocatalytic Properties of a Cu Electrode with Organic Additives Containing Amine Group for CO2 Reduction. *J. Mater. Chem. A* **2019**, *7*, 5453-5462.

52.   Xie, M. S.; Xia, B. Y.; Li, Y.; Yan, Y.; Yang, Y.; Sun, Q.; Chan, S. H.; Fisher, A.; Wang, X., Amino Acid Modified Copper Electrodes for the Enhanced Selective Electroreduction of Carbon Dioxide towards Hydrocarbons. *Energy Environ. Sci.* **2016**, *9*, 1687-1695.

53.   Banerjee, S.; Han, X.; Thoi, V. S., Modulating the Electrode-Electrolyte Interface with Cationic Surfactants in Carbon Dioxide Reduction. *ACS Catal.* **2019**, *9*, 5631-5637.

54.   Zhang, Z.-Q.; Banerjee, S.; Thoi, V. S.; Shoji Hall, A., Reorganization of Interfacial Water by an Amphiphilic Cationic Surfactant Promotes CO2 Reduction. *J. Phys. Chem. Lett.* **2020**, *11*, 5457-5463.

55.   Osowiecki, W. T.; Ye, X.; Satish, P.; Bustillo, K. C.; Clark, E. L.; Alivisatos, A. P., Tailoring Morphology of Cu–Ag Nanocrescents and Core–Shell Nanocrystals Guided by a Thermodynamic Model. *J. Am. Chem. Soc.* **2018**, *140*, 8569-8577.

56.   Kamat, G. A.; Yan, C.; Osowiecki, W. T.; Moreno-Hernandez, I. A.; Ledendecker, M.; Alivisatos, A. P., Self-Limiting Shell Formation in Cu@Ag Core–Shell Nanocrystals during Galvanic Replacement. *J. Phys. Chem. Lett.* **2020**, *11*, 5318-5323.

57.   Song, J. T.; Li, H. Y.; Li, J.; Wang, S. Y.; Zhou, S. M., Fabrication and Optical Properties of Metastable Cu-Ag Alloys. *Appl. Opt.* **2002**, *41*, 5413-5416.

58.   Nilsson, P.; Forssell, G., Optical Properties of Metastable One Phase Cu-Ag Alloys. *Le Journal de Physique Colloques* **1974**, *35*, C4-57-C4-59.

59.   Tariq, M.; Koch, M. D.; Andrews, J. W.; Knowles, K. E., Correlation between Surface Chemistry and Optical Properties in Colloidal Cu2O Nanoparticles. *J. Phys. Chem. C* **2020**, *124*, 4810-4819.

60.   Midgley, P. A.; Weyland, M., 3D Electron Microscopy in the Physical Sciences: The Development of Z-Contrast and EFTEM Tomography. *Ultramicroscopy* **2003**, *96*, 413-431.

61.   Blommaerts, N.; Vanrompay, H.; Nuti, S.; Lenaerts, S.; Bals, S.; Verbruggen, S. W., Unraveling Structural Information of Turkevich Synthesized Plasmonic Gold–Silver Bimetallic Nanoparticles. *Small* **2019**, *15*, 1902791.

62.   Muzikansky, A.; Nanikashvili, P.; Grinblat, J.; Zitoun, D., Ag Dewetting in Cu@ Ag Monodisperse Core–Shell Nanoparticles. *J. Phys. Chem. C* **2013**, *117*, 3093-3100.

63.   Dai, X.; Xu, W.; Zhang, T.; Shi, H.; Wang, T., Room Temperature Sintering of Cu-Ag Core-Shell Nanoparticles Conductive Inks for Printed Electronics. *Chem. Eng. J.* **2019**, *364*, 310-319.

64.   Tang, L.; Wu, W.; He, L.; Yu, K.; Xu, T.; Zhang, Q.; Zhang, L.; Sun, L., Novel Interface in CuAg Nanostructure Induced by Size Effect. *J. Phys. Chem. Lett.* **2019**, *10*, 1973-1980.

65.   Yuan, C.; Shin, S.; Liao, C.; Guzman, J.; Stone, P.; Watanabe, M.; Ager III, J.; Haller, E.; Chrzan, D., Structure Map for Embedded Binary Alloy Nanocrystals. *Appl. Phys. Lett.* **2008**, *93*, 193114.

66.   Dettelbach, K. E.; He, J. F.; Johnson, N. J. J.; Huang, A. X.; Bottomley, A.; Lam, B.; Salvatore, D. A.; Berlinguette, C. P., Kinetic Phases of Ag-Cu Alloy Films are Accessible through Photodeposition. *J. Mater. Chem. A* **2019**, *7*, 711-715.

67.   Biesinger, M. C., Advanced Analysis of Copper X-Ray Photoelectron Spectra. *Surf. Interface Anal.* **2017**, *49*, 1325-1334.

68.   Singh, M. R.; Kwon, Y.; Lum, Y.; Ager, J. W.; Bell, A. T., Hydrolysis of Electrolyte Cations Enhances the Electrochemical Reduction of CO2 over Ag and Cu. *J. Am. Chem. Soc.* **2016**, *138*, 13006-13012.

69.   Clark, E. L.; Ringe, S.; Tang, M.; Walton, A.; Hahn, C.; Jaramillo, T. F.; Chan, K.; Bell, A. T., Influence of Atomic Surface Structure on the Activity of Ag for the Electrochemical Reduction of CO2 to CO. *ACS Catal.* **2019**, *9*, 4006-4014.

70.   Wang, R.; Haspel, H.; Pustovarenko, A.; Dikhtiarenko, A.; Russkikh, A.; Shterk, G.; Osadchii, D.; Ould-Chikh, S.; Ma, M.; Smith, W. A.; Takanabe, K.; Kapteijn, F.; Gascon, J., Maximizing Ag Utilization in High-Rate CO2 Electrochemical Reduction with a Coordination Polymer-Mediated Gas Diffusion Electrode. *ACS Energy Lett.* **2019**, *4*, 2024-2031.

71.   Rosen, J.; Hutchings, G. S.; Lu, Q.; Rivera, S.; Zhou, Y.; Vlachos, D. G.; Jiao, F., Mechanistic Insights into the Electrochemical Reduction of CO2 to CO on Nanostructured Ag Surfaces. *ACS Catal.* **2015**, *5*, 4293-4299.

72.   Back, S.; Yeom, M. S.; Jung, Y., Active Sites of Au and Ag Nanoparticle Catalysts for CO2 Electroreduction to CO. *ACS Catal.* **2015**, *5*, 5089-5096.

73.	Schmitt, K. G.; Gewirth, A. A., *In Situ* Surface-Enhanced Raman Spectroscopy of the Electrochemical Reduction of Carbon Dioxide on Silver with 3,5-Diamino-1,2,4-Triazole. *J. Phys. Chem. C* **2014**, *118*, 17567-17576.

74.	Mistry, H.; Behafarid, F.; Reske, R.; Varela, A. S.; Strasser, P.; Roldan Cuenya, B., Tuning Catalytic Selectivity at the Mesoscale *via* Interparticle Interactions. *ACS Catal.* **2016**, *6*, 1075-1080.

75.	Osowiecki, W. T.; Nussbaum, J. J.; Kamat, G. A.; Katsoukis, G.; Ledendecker, M.; Frei, H.; Bell, A. T.; Alivisatos, A. P., Factors and Dynamics of Cu Nanocrystal Reconstruction under CO2 Reduction. *ACS Appl. Energ. Mater.* **2019**, *2*, 7744-7749.

76.	Kim, D.; Kley, C. S.; Li, Y.; Yang, P., Copper Nanoparticle Ensembles for Selective Electroreduction of CO2 to C2–C3 Products. *Proc. Natl. Acad. Sci. U. S. A.* **2017**, *114*, 10560-10565.

77.	Ma, M.; Clark, E. L.; Therkildsen, K. T.; Dalsgaard, S.; Chorkendorff, I.; Seger, B., Insights into the Carbon Balance for CO2 Electroreduction on Cu Using Gas Diffusion Electrode Reactor Designs. *Energy Environ. Sci.* **2020**, *13*, 977-985.

78.	Higgins, D.; Hahn, C.; Xiang, C.; Jaramillo, T. F.; Weber, A. Z., Gas-Diffusion Electrodes for Carbon Dioxide Reduction: A New Paradigm. *ACS Energy Lett.* **2019**, *4*, 317-324.

79.	Liu, K.; Smith, W. A.; Burdyny, T., Introductory Guide to Assembling and Operating Gas Diffusion Electrodes for Electrochemical CO2 Reduction. *ACS Energy Lett.* **2019**, *4*, 639-643.

80.	Zhang, J.; Luo, W.; Züttel, A., Crossover of Liquid Products from Electrochemical CO2 Reduction through Gas Diffusion Electrode and Anion Exchange Membrane. *J. Catal.* **2020**, *385*, 140-145.

81.	Gupta, N.; Gattrell, M.; MacDougall, B., Calculation for the Cathode Surface Concentrations in the Electrochemical Reduction of CO2 in KHCO3 Solutions. *J. Appl. Electrochem.* **2006**, *36*, 161-172.

82.	Zhang, M.-K.; Chen, W.; Xu, M.-L.; Wei, Z.; Zhou, D.; Cai, J.; Chen, Y.-X., How Buffers Resist Electrochemical Reaction-Induced pH Shift under a Rotating Disk Electrode Configuration. *Anal. Chem.* **2021**, *93*, 1976-1983.

83.	Gutiérrez-Sánchez, O.; Daems, N.; Offermans, W.; Birdja, Y. Y.; Bulut, M.; Pant, D.; Breugelmans, T., The Inhibition of the Proton Donor Ability of Bicarbonate Promotes the Electrochemical Conversion of CO2 in Bicarbonate Solutions. *J. CO2 Util.* **2021**, *48*, 101521.

84.	Clark, E. L.; Wong, J.; Garza, A. J.; Lin, Z.; Head-Gordon, M.; Bell, A. T., Explaining the Incorporation of Oxygen Derived from Solvent Water into the Oxygenated Products of CO Reduction over Cu. *J. Am. Chem. Soc.* **2019**, *141*, 4191-4193.

85.	Birdja, Y. Y.; Koper, M. T. M., The Importance of Cannizzaro-Type Reactions during Electrocatalytic Reduction of Carbon Dioxide. *J. Am. Chem. Soc.* **2017**, *139*, 2030-2034.

86.	Kuhl, K. P.; Cave, E. R.; Abram, D. N.; Jaramillo, T. F., New Insights into the Electrochemical Reduction of Carbon Dioxide on Metallic Copper Surfaces. *Energy Environ. Sci.* **2012**, *5*, 7050-7059.

87.	Schouten, K. J. P.; Kwon, Y.; van der Ham, C. J. M.; Qin, Z.; Koper, M. T. M., A New Mechanism for the Selectivity to C1 and C2 Species in the Electrochemical Reduction of Carbon Dioxide on Copper Electrodes. *Chem. Sci.* **2011**, *2*, 1902-1909.

88.	Hanselman, S.; Koper, M. T. M.; Calle-Vallejo, F., Computational Comparison of Late Transition Metal (100) Surfaces for the Electrocatalytic Reduction of CO to C2 Species. *ACS Energy Lett.* **2018**, *3*, 1062-1067.

89.	Clark, E. L.; Hahn, C.; Jaramillo, T. F.; Bell, A. T., Electrochemical CO2 Reduction over Compressively Strained CuAg Surface Alloys with Enhanced Multi-Carbon Oxygenate Selectivity. *J. Am. Chem. Soc.* **2017**, *139*, 15848-15857.

90.	Wang, L.; Higgins, D. C.; Ji, Y.; Morales-Guio, C. G.; Chan, K.; Hahn, C.; Jaramillo, T. F., Selective Reduction of CO to Acetaldehyde with CuAg Electrocatalysts. *Proc. Natl. Acad. Sci. U. S. A.* **2020**, *117*, 12572.

91.	Li, Y. G. C.; Wang, Z. Y.; Yuan, T. G.; Nam, D. H.; Luo, M. C.; Wicks, J.; Chen, B.; Li, J.; Li, F. W.; de Arguer, F. P. G.; Wang, Y.; Dinh, C. T.; Voznyy, O.; Sinton, D.; Sargent, E. H., Binding Site Diversity Promotes CO2 Electroreduction to Ethanol. *J. Am. Chem. Soc.* **2019**, *141*, 8584-8591.

92.	Hoang, T. T. H.; Verma, S.; Ma, S.; Fister, T. T.; Timoshenko, J.; Frenkel, A. I.; Kenis, P. J. A.; Gewirth, A. A., Nanoporous Copper–Silver Alloys by Additive-Controlled Electrodeposition for the Selective Electroreduction of CO2 to Ethylene and Ethanol. *J. Am. Chem. Soc.* **2018**, *140*, 5791-5797.

93.   Huang, J.; Mensi, M.; Oveisi, E.; Mantella, V.; Buonsanti, R., Structural Sensitivities in Bimetallic Catalysts for Electrochemical CO2 Reduction Revealed by Ag–Cu Nanodimers. *J. Am. Chem. Soc.* **2019**, *141*, 2490-2499.

94.   Chen, C.; Li, Y.; Yu, S.; Louisia, S.; Jin, J.; Li, M.; Ross, M. B.; Yang, P., Cu-Ag Tandem Catalysts for High-Rate CO2 Electrolysis toward Multicarbons. *Joule* **2020**, *4*, 1688-1699.

95.   Wang, X. L.; de Araujo, J. F.; Ju, W.; Bagger, A.; Schmies, H.; Kuhl, S.; Rossmeisl, J.; Strasser, P., Mechanistic Reaction Pathways of Enhanced Ethylene Yields during Electroreduction of CO2-CO Co-feeds on Cu and Cu-Tandem Electrocatalysts. *Nat. Nanotechnol.* **2019**, *14*, 1063-+.

96.   Ting, L. R. L.; Piqué, O.; Lim, S. Y.; Tanhaei, M.; Calle-Vallejo, F.; Yeo, B. S., Enhancing CO2 Electroreduction to Ethanol on Copper–Silver Composites by Opening an Alternative Catalytic Pathway. *ACS Catal.* **2020**, *10*, 4059-4069.

97.   Iyengar, P.; Kolb, M. J.; Pankhurst, J. R.; Calle-Vallejo, F.; Buonsanti, R., Elucidating the Facet-Dependent Selectivity for CO2 Electroreduction to Ethanol of Cu-Ag Tandem Catalysts. *ACS Catal.* **2021**, *11*, 4456-4463.

98.   Hori, Y.; Takahashi, R.; Yoshinami, Y.; Murata, A., Electrochemical Reduction of CO at a Copper Electrode. *J. Phys. Chem. B* **1997**, *101*, 7075-7081.

99.   Ren, D.; Ang, B. S.-H.; Yeo, B. S., Tuning the Selectivity of Carbon Dioxide Electroreduction toward Ethanol on Oxide-Derived CuxZn Catalysts. *ACS Catal.* **2016**, *6*, 8239-8247.

100.   Singh, M. R.; Clark, E. L.; Bell, A. T., Effects of Electrolyte, Catalyst, and Membrane Composition and Operating Conditions on the Performance of Solar-Driven Electrochemical Reduction of Carbon Dioxide. *Phys. Chem. Chem. Phys.* **2015**, *17*, 18924-18936.

101.   Hung, L.-I.; Tsung, C.-K.; Huang, W.; Yang, P., Room-Temperature Formation of Hollow Cu2O Nanoparticles. *Adv. Mater.* **2010**, *22*, 1910-1914.

102.   Yin, M.; Wu, C.-K.; Lou, Y.; Burda, C.; Koberstein, J. T.; Zhu, Y.; O'Brien, S., Copper Oxide Nanocrystals. *J. Am. Chem. Soc.* **2005**, *127*, 9506-9511.

103.   Li, C.; Tardajos, A. P.; Wang, D.; Choukroun, D.; Van Daele, K.; Breugelmans, T.; Bals, S., A Simple Method to Clean Ligand Contamination on TEM Grids. *Ultramicroscopy* **2021**, *221*, 113195.

104.   Schlossmacher, P.; Klenov, D. O.; Freitag, B.; von Harrach, H. S., Enhanced Detection Sensitivity with a New Windowless XEDS System for AEM Based on Silicon Drift Detector Technology. *Microsc. Today* **2010**, *18*, 14-20.

105.   Legland, D.; Arganda-Carreras, I.; Andrey, P., MorphoLibJ: Integrated Library and Plugins for Mathematical Morphology with ImageJ. *Bioinformatics* **2016**, *32*, 3532-3534.

TOC Graphic